NEUROPEPTIDE SIGNALING IS REQUIRED TO IMPLEMENT A LINE ATTRACTOR ENCODING A PERSISTENT INTERNAL BEHAVIORAL STATE

George Mountoufaris[1,3], Aditya Nair[1,2], Bin Yang[5], Dong-Wook Kim[6] and David J. Anderson[1,3,4,*]

[1]Division of Biology and Biological Engineering

[2]Program in Computation and Neural Systems

[3]Tianqiao and Chrissy Chen Institute for Neuroscience

California Institute of Technology

[4]Howard Hughes Medical Institute

Pasadena, CA 91001

[5]Present address: Johns Hopkins University School of Medicine

[6]Present address: Allen Institute for Brain Science

Running title: Neuropeptides control attractor dynamics

***Author for correspondence**

Tel (o): (626) 395-6821/8374

wuwei@caltech.edu

lchavarr@caltech.edu

ABSTRACT

Internal states drive survival behaviors, but their neural implementation is not well understood. Recently we identified a line attractor in the ventromedial hypothalamus (VMH) that represents an internal state of aggressiveness. Line attractors can be implemented by recurrent connectivity and/or neuromodulatory signaling, but evidence for the latter is scant. Here we show that neuropeptidergic signaling is necessary for line attractor dynamics in this system, using a novel approach that integrates cell type-specific, anatomically restricted CRISPR/Cas9-based gene editing with microendoscopic calcium imaging. Co-disruption of receptors for oxytocin and vasopressin in adult VMH Esr1^{+} neurons that control aggression suppressed attack, reduced persistent neural activity and eliminated line attractor dynamics, while only modestly impacting neural activity and sex- or behavior-tuning. These data identify a requisite role for neuropeptidergic signaling in implementing a behaviorally relevant line attractor. Our approach should facilitate mechanistic studies in neuroscience that bridge different levels of biological function and abstraction.

Introduction

Innate survival behaviors such as aggression, mating, feeding and defense are driven by internal motivational or emotion states[1-3], which are experienced in humans as subjective feelings[4,5]. How and where such internal states are encoded in the brain, and how they are causally related to overt behavior, is emerging as a major topic in circuit and systems neuroscience[6,7].

The study of internal states has been pursued via two general lines of research that have until recently remained relatively separate. One, a "bottom-up" approach, is grounded in perturbational studies and has focused on genetically or pharmacologically based manipulations of genes (e.g., neuromodulators) and neural circuits[6,8,9] aimed at providing causal explanations for behavioral, psychological or homeostatic internal states[10-12]. The other, a "top-down" approach, is grounded in observational studies, and has defined internal states mathematically through modeling of high-dimensional neural population activity[13,14]. Dynamical system models of low-dimensional neural activity have revealed features such as attractors and integrators that appear to underly many cognitive functions[15-18]. More recently, such models have been applied in behavioral neuroscience as well[19-21]. To test the causal role of such emergent network properties in behavior it is important to understand their neural implementation at the level of specific cell types. This in turn requires integration of these two approaches[22]. Such an integrated approach has thus far been accomplished in very few systems[23,24].

One important implementation question concerns the mechanism(s) that control slow neural dynamics. Persistent neural activity (on a timescale of seconds to minutes) is a characteristic feature of neural integrators and attractor dynamics[17,25,26]. Two alternative (but not mutually exclusive) implementation mechanisms are typically invoked to explain such persistence: recurrent fast synaptic connectivity or slow neuromodulation[27]. While there is EM connectomic

60 evidence of recurrent connectivity underlying a ring attractor that encodes head direction in
61 *Drosophila*[23,24,28], to our knowledge there is no evidence of any neuromodulator that controls
62 attractor dynamics in any system.

63 Neuropeptides comprise a class of evolutionarily conserved[29,30] neuromodulators that control
64 behavior-specific internal motive states associated with mating[31,32], aggression[33-35], social
65 attachment[36], feeding[37] and predator defense[38], as well as other behaviors. Neuropeptides are well
66 known to modulate synaptic strength and neural circuit properties such as patterns of oscillation[39-
67 41], but their role in implementing persistent activity and attractor dynamics has not been
68 extensively studied in vertebrates. Experiments in *C. elegans* have uncovered the circuit
69 architecture through which neuropeptides control persistent states of locomotor activity[42,43], but
70 whether they influence population dynamics manifolds identified in that system[44] is not yet clear.

71 A powerful approach to this question is to integrate specific pharmacological or genetic
72 perturbations of neuromodulatory signaling with simultaneous large-scale recording of neural
73 activity in the same brain region and genetically defined cell type. While this integration has been
74 achieved at the brain-wide scale in *C. elegans*[45] and larval zebrafish[46], with few exceptions[47] it has
75 been difficult to implement in mammalian systems, largely for technical reasons (Supplemental
76 Figure 1A).

77 Here we describe a novel viral-based strategy that integrates cell type-specific CRISPR/Cas9-
78 based multiplex gene editing[48] with single unit-resolution calcium imaging in freely behaving adult
79 animals[49], which we call "CRISPRoscopy". This method, when combined with dynamical systems
80 modeling, allows investigation of the effects of local inactivation of different neuromodulatory
81 systems on neural population coding, dynamics and behavior, in the same brain region and cell
82 type.

83 As a proof-of-concept application of this approach, we have examined the role of oxytocin
84 (OXT) and arginine vasopressin (AVP) signaling in a population of ventromedial hypothalamic
85 (VMH) neurons that control aggression[50]. We chose this testbed for several reasons. First, these
86 neuropeptides have been widely implicated in the control of social behaviors[36,51] (although the role
87 of OXT in aggression has been controversial)[52]. Second, aggression is a robust, naturalistic,
88 evolutionarily conserved and innate social behavior[53]. Third, anatomically restricted[54] and
89 genetically defined[55,56] VMH cell populations that play a causal role in aggression have been
90 identified and their activity imaged during aggressive encounters[57-59]. Fourth, VMH neurons are
91 known to express receptors for OXT and AVP[60,61] and infusion of the latter peptide into VMH can
92 enhance aggression in hamsters[62]. Finally, recent application of dynamical systems modeling[63] to
93 population recordings from these neurons has revealed an approximate line attractor that represents
94 a scalable and persistent internal state of aggressiveness[20].

95 Due to ligand cross-talk[64] and potential genetic redundancy between *Oxtr* and *Avpr1a*, as a
96 first step to applying this technology we elected to simultaneously edit both genes. We found that
97 genetically disrupting both receptors in VMHvl^{Esr1} neurons[55] strongly reduced the intensity and
98 frequency of attack behavior, but caused only a modest reduction in overall neuronal activity, and
99 population coding of behavior and intruder sex[59]. In contrast, it strongly reduced persistent neural
100 activity. Dynamical systems modeling revealed that the line attractor was replaced by a slow point
101 corresponding to the animals' resting state. These data provide the first evidence in any system of
102 a requirement for neuropeptide signaling in the implementation of an attractor.

103 **Results**

104 **Most Esr1^{+} neurons co-express Oxytocin and Vasopressin receptors and respond to these**
105 **peptides *ex vivo***

106 The expression of Oxtr and Avpr1a has been extensively mapped in the brains of multiple
107 species by radioligand binding, in situ hybridization and knock-in reporters[60,61,65-68]. To determine
108 whether these receptors are co-expressed in individual VMH neurons we examined a single cell
109 RNAseq (scRNAseq)-based atlas of VMHvl transcriptomic cell types anatomically validated by
110 smFISH[69]. We observed co-expression of *Oxtr* and *Avpr1α* mRNA transcripts (but not of *Avpr1β*
111 or *Avp2r* transcripts) within individual neurons belonging to several $Esr1^+$ transcriptomic clusters
112 (Figure 1B and Supplemental Figure S1B, E). All $Esr1^+$ VMHvl clusters contained cells expressing
113 *Oxtr*, with most clusters (5/8) containing cells that co-expressed *Avpr1a* transcripts (Figure 1C-D
114 and Supplemental Figure S1C). Overall, ~78% of $Esr1^+$ cells in VMHvl expressed Oxtr mRNA,
115 and ~61% of these cells also expressed Avpr1a mRNAs (Figure 1E). However, none of the VMHvl
116 clusters expressed *Oxt* or *Avp* transcripts, indicating that the source(s) of the peptides must be
117 extrinsic to the nucleus (Supplemental Figure S1D).

118 To explore the effect of OXT and AVP on the physiological activity of VMHvl neurons,
119 we used a system for 2-photon imaging system of acute VMH slice preparations[55] (Figure 1Fi).
120 This system enabled us to record Ca^{2+} traces in brain slices from ESR1-2A-CRE animals[55]
121 expressing a CRE-dependent Ca^{2+} indicator (GCaMP7f)[70]. Perfusing a mixture of 400nM (each)
122 OXT plus AVP or individually administering these peptides elicited strong ($\Delta F/F$ ~500-600%)
123 responses in $VMHvl^{Esr1}$ cells (Figure 1Fii and Supplemental Figure S1F-G). These findings
124 demonstrated the presence of functional AVP and OXT receptors in $VMHvl^{Esr1}$ neurons, consistent
125 with prior electrophysiological studies in mice and guinea pigs[71,72]. Furthermore, it established a
126 system for evaluating cellular responses to OXT and AVP following CRISPR/Cas9 based
127 mutations of their receptors.

128 **Oxtr/Avpr1a-mediated neuropeptidergic signaling in VMH is required for male territorial**
129 **aggression**

130 The likelihood of functional redundancy or developmental compensation between OXTR
131 and AVPR1a in mediating responses to OXT and/or AVP[64,71] prompted us to design a multiplex
132 viral CRISPR/Cas9 approach to concurrently target both receptors in the same cells. To do this,
133 we modified previously described vectors[73] to express two different gRNAs targeting *Oxtr* and
134 *Avpr1a* from four distinct Pol III promoters in either a lentiviral (LV) or an AAV vector (Figure
135 2A; see Methods). We used two different gRNAs for each receptor gene since this approach has
136 been reported to significantly increase *in vivo* gene editing efficiency in the mammalian nervous
137 system[74]. Each gRNA was designed to target either the *Oxtr* or the *Avpr1a* coding region, and this
138 specificity was confirmed using the T7 endonuclease assay[75] (Supplemental Figure S2A).

139 While OXT, AVP and their receptors have been studied extensively in rodent aggression
140 using pharmacologic reagents and organismal gene knockouts,[31,52,76-79] there are no reports of a
141 specific requirement in offensive aggression for either *Oxtr* and/or *Avpr1a* in murine VMH.
142 Because pharmacological blockers are difficult to restrict to small anatomical regions due to
143 diffusion that cannot be visualized following injection, we initially sought to use CRISPR/Cas9-
144 mediated gene editing to evaluate whether these receptors are functionally relevant to this behavior
145 in VMH *in vivo*. Generating viruses with the high titers necessary for *in vivo* applications (see
146 Methods) precluded the inclusion of a Cas9 cDNA in the same vector that encoded two different
147 gRNAs each against *Oxtr* and *Avpr1a*. Therefore, Cas9 was delivered by co-injection of a separate
148 AAV (Figure 2Aii). To target VMHvl neurons broadly for this initial experiment, we employed a
149 constitutive version of the system. We used a LV-based vector to express the 4 different gRNAs,
150 because we found that its anatomical spread is more restricted than that of AAVs.

151 Examination of hypothalamic sections from animals co-injected with the gRNA-DsRed
152 LV and the Cas9 AAV using DsRed fluorescence and anti-Cas9 immunostaining indicated that
153 ~80% of $Cas9^+$ cells were co-infected with the gRNA virus (Figure 2C, D). Assessing the
154 efficiency of co-disrupting both receptors *in vivo* at the protein level was not feasible due to a lack
155 of equally specific immune reagents for both OXTR and AVPR1a. Furthermore, because the small
156 1-2 nucleotide DNA insertions or deletions (INDELs) created by CRISPR/Cas9 editing do not
157 necessarily result in reduced levels of mRNA expression from the targeted genes[80], assessing
158 editing by *in situ* hybridization is not a reliable indicator of targeting efficiency. As described in
159 the next section, we tested the functional efficacy of *Oxtr/Avpr1a* co-editing via calcium imaging
160 in acute VMH brain slices, and indeed found a strong suppression of physiological responses to
161 OXT+AVP (Supplementary Figure S3B and Figure 3A).

162 Next, we examined social behaviors in mice injected in VMH bilaterally with the OAR-
163 gRNA LV and a Cas9 AAV, using a standard resident intruder (RI) assay (Figure 1A). We used
164 single-housed, sexually experienced wild-type C57BL/6N resident males pre-selected for adequate
165 aggressiveness (Figure 2E, see Methods). Control animals were co-injected bilaterally with the
166 scrambled gRNA (Scr gRNA) and Cas9 viruses. Experimental mice displayed a notable reduction
167 in aggression towards male intruders, as evidenced by significant decreases in the number and
168 time-varying probability of attack bouts, the total time spent attacking and the average duration of
169 each attack bout; in addition, the latency to the 1st attack bout was significantly increased (Figure
170 2Fi-ii and Supplemental Figure S2B, Ci, ii). These behavioral effects were not due to defects in
171 locomotor activity since average velocity during attack episodes was similar between experimental
172 and control mice (Supplemental Figure S2Ciii). In contrast, the time spent in close investigation
173 (sniffing) of male intruders did not differ significantly between experimental and control male

174 residents (Figure 2Fiii). Experimental males also did not differ significantly from controls in their
175 sniffing or mounting behavior towards female intruders (Figure 2G and Supplemental Figure
176 S2D).

177 These data suggest that *Oxtr* and/or *Avpr1a* expressed in VMHvl neurons play a requisite
178 and selective role in aggressive behavior. Furthermore, they motivated us to analyze next how
179 disrupting these receptors specifically in Esr1 neurons affects behavior, neural activity, population
180 coding and network dynamics *in vivo*.

181

182 **Altered VMHvl^{Esr1} neural activity during social interactions in mice with perturbed**
183 **OXT/AVP signaling**

184 Male VMHvl^{Esr1} neural activity normally increases during sniffing and attack towards an
185 intruder male[57,59,81]. We therefore sought to analyze the activity of these neurons via calcium
186 imaging in mice with or without co-disruption of *Oxtr* and *Avpr1a*. To restrict CRISPR-based gene
187 editing to the same cell population that we wished to image, we constructed an AAV vector that
188 encodes both the gRNAs and a Cre-dependent GCaMP8s (Figure 3A, upper). In mice co-injected
189 with a Cre-dependent Cas9 AAV, cells co-infected with both viruses are expected to undergo gene
190 editing. The use of Cre-dependent AAVs in these experiments yields higher levels of expression
191 than LVs as well as cell type specificity. Double-labeling with antibodies to GFP (GCaMP8s) and
192 Cas9 in mice co-injected with the two Cre-dependent AAVs (Figure 3A) indicated that ~66% of
193 GCaMP8s-expressing Esr1 neurons were Cas9^{+} (Supplementary Figure S3Ai-ii).

194 As mentioned above, *in vivo* quantification of the frequency and efficiency of *Oxtr/Avpr1a*
195 gene disruption on a cell-by-cell basis (either by immune-labeling *or in situ* hybridization) was
196 precluded for technical reasons. As an alternative approach to verify the disruption of normal

197 signaling responses to OXT and AVP in Esr1 neurons with co-targeting of *Oxtr* and *Avpr1a*, we
198 performed *ex vivo* calcium imaging of VMH slices (Figure 1Fi) from ESR1-2A-CRE mice co-
199 injected with the Cas9 and Cre-dependent gRNAs-GCaMP8s viruses (Figure 3Ai). Physiological
200 responses to the application of mixed AVP and OXT peptides were significantly attenuated (~2.5-
201 fold) in slices from experimental mice expressing *Oxtr/Avpr1a* gRNAs in $Esr1^{+}$ cells, compared
202 to slices from control mice expressing a scrambled (Scr) gRNA in these cells (Supplementary
203 Figure S3B). Thus, co-disruption of *Oxtr/Avpr1a* using our dual viral-based CRISPR/Cas9 system
204 can reduce physiological responses to OXT and AVP in $VMHvl^{Esr1}$ neurons, although they do not
205 eliminate such responses completely.

206 We next used the Cre-dependent gene editing and GCaMP imaging system to test whether
207 *Oxtr/Avpr1a* mediated signaling is required selectively in Esr1 neurons during aggression, and to
208 examine simultaneously how neural activity in these cells is affected. Similar to the results
209 obtained initially with the Cre-independent system, bilateral co-disruption of *Oxtr/Avpr1a* in
210 $VMHvl^{Esr1}$ neurons significantly reduced most metrics of aggression towards male intruder
211 compared to control mice, although to a somewhat lower extent (Figure 3Ci, ii; Supplementary
212 Figure 3C). Using fiber photometry to measure bulk calcium signals (Figure 3B, C), we observed
213 a significant reduction in overall $VMHvl^{Esr1}$ neuronal activity during the infrequent attack bouts
214 exhibited by experimental mice (Figure 3G, compare red vs. grey rasters) (Figure 3H). A reduction
215 in $VMHvl^{Esr1}$ activity during sniffing episodes was also observed in these mice (Figure 3E-F), even
216 though the duration of investigative behavior remained unaffected (Figure 3Ciii). In contrast,
217 during male-female interactions, calcium signals in experimental males were not significantly
218 different from controls (Supplementary Figure S3E-F), consistent with the lack of an effect on
219 mounting behavior (Figure 3D; Supplementary Figure S3D). Thus, males with bilateral co-

220 disruption of Oxtr/Avpr1a-mediated signaling in VMHvl^{Esr1} neurons exhibited a reduction in both
221 aggression and neural activity. However, these data did not distinguish whether the reduced
222 activity was a cause or a consequence of the diminished aggressive behavior.
223
224 **Single cell "CRISPRscope" imaging of VMHvl^{Esr1} neurons with co-disruption of *Oxtr/Avpr1a***
225 To investigate how co-editing of *Oxtr/Avpr1a* affects activity in individual VMHvl^{Esr1}
226 neurons, we imaged Ca^{2+} activity using a miniature head-mounted microscope[49] in Esr1-2A-CRE
227 males co-injected with the experimental or control virus pairs. We call this approach
228 "CRISPRoscopy." Because there are virtually no commissural connections between VMHvl[58],
229 unilateral loss-of-function manipulations of this nucleus are typically compensated by the
230 unmanipulated side. To avoid any influence on neural activity of reduced aggressive behavior
231 caused by *Oxtr/Avpr1a* co-disruption, we performed calcium imaging and functional perturbations
232 unilaterally in freely behaving animals (Figure 4A), a previously validated strategy[58] .
233
234 **Effect of Oxtr/Avpr1a co-editing on intruder sex-specific representations during social**
235 **encounters**
236 Our previous single unit calcium imaging studies have shown that in socially experienced
237 males VMHvl contains distinct Esr1^{+} neural ensembles activated in the presence of males vs.
238 females, with some units showing mixed sex-selectivity [2,57-59]. This separation was also clear in
239 raster plots of VMHvl^{Esr1} units imaged in control vs experimental males (Figure 4B). To quantify
240 the proportion of sex-preferring neurons, we measured unit activity during the first two minutes
241 after the introduction of a male or female intruder in two ways: either by z-scoring (relative to the

242 cell's mean fluorescence over the entire recording period), or by the change in fluorescence relative
243 to the mean pre-intruder baseline [57,58] (in units of σ; see Methods).

244 During interactions with a male intruder, the experimental cumulative distribution function
245 (ECDF) and mean activity of all units (pooled from n=4 control and n=7 experimental animals)
246 were slightly but significantly decreased in experimental mice (Figure 4Ei, Fi; Supplementary
247 Figure 4Ci). However, the mean activity among cells considered as "active" (≥ 2σ above
248 baseline[59]) did not differ between control and experimental mice (Supplemental Figure S4D).
249 During interactions with females there was no significant difference in activity (measured in σ
250 above baseline) between experimental and control animals (Figure 4Eii, Fii), although z-scored
251 activity showed a slight but significant increase (Supplementary Figure 4Cii).

252 Next, we measured the percentage of male-selective (activity ≥ 2σ during male but not
253 female interactions) and mixed selectivity (activity ≥ 2σ during both male and female interactions)
254 neurons within the $Esr1^+$ population during male-male interactions. The combined percentage of
255 all male-activated neurons was slightly smaller in experimental than control mice (34.6% vs.
256 38.3%, respectively; Figure 4G and Supplemental Figure S4E), while there was a ~56% reduction
257 in the fraction of male-selective neurons (6.3 □ 2% vs. 14.4 □ 4%, respectively; Figure 4G).
258 Conversely, during female interactions the fraction of female-selective and mixed selectivity
259 neurons was increased by ~4% and ~44%, respectively, in experimental mice (Figure 4G and
260 Supplemental Figure S4E). Together these data are suggestive of a shift in sex-specific tuning from
261 male-selective to mixed selectivity, a conclusion consistent with choice probability analysis (see
262 below).

263 To determine whether this shift affected the ability to accurately decode intruder sex at the
264 population level, we performed dimensionality reduction using partial least-squares (PLS)

265 regression. This analysis revealed a clear separation of responses during encounters with males vs.
266 females in both control and experimental animals (Figure 4C; Supplemental Figure S4A-B). In
267 addition, linear SVM decoders trained on imaging data from either control or experimental mice
268 correctly predicted intruder sex with virtually 100% accuracy (Figure 4D). Thus in socially
269 experienced animals, co-targeting of *Oxtr*/*Avpr1a* in VMHvl^{Esr1} cells does not disrupt the
270 population coding of intruder sex[59], despite the altered sex-selectivity of some of these units.
271

272 **Social behavior-selective tuning of VMHvl^{Esr1} neurons with co-disruption of *Oxtr*/*Avpr1a***

273 Next, we examined the effect of co-disruption of *Oxtr/Avpr1a* on VMHvl^{Esr1} neuronal
274 activity during the different behavioral phases of social interactions with males or females:
275 appetitive (sniffing) or consummatory (attack or mounting, respectively). The ECDF and average
276 single unit activity during male-directed sniffing or attack was slightly but significantly lower in
277 experimental than in control mice (Figure 5Ai, ii, Ci, ii and Supplementary Figure S5Ai, Bi-ii). In
278 contrast, during social interactions with females' activity during sniffing and mounting was similar
279 (Figure 5Aiii, iv, Ciii, iv and Supplementary Figure S5Biii-iv). As an additional approach, we
280 quantified the average activity in peri-event time histograms (PETHs) for each type of behavior
281 after subtracting the pre-behavior baseline, using z-scored data (see Methods). The mean activity
282 during male-directed sniffing or attack was slightly but significantly lower in experimental than in
283 control mice (Supplemental Figure S5Ci, ii), while it was significantly higher during female-
284 directed sniffing, but unchanged during mounting (Supplemental Figure S5Ciii, iv). In summary,
285 the activity of VMHvl^{Esr1} units during different social behaviors was either unchanged or only
286 slightly different between experimental and control animals, with minor decreases or increases
287 during male- vs. female-directed behaviors, respectively.

288 We next examined the proportion of behavior-selective units (defined as units with activity
289 ≥ 2σ above pre-intruder baseline during, e.g., sniff but not attack or vice-versa)[57-59]. As we
290 previously showed, a relatively small fraction of VMHvl^{Esr1} neurons was selective for sniff or
291 attack (~2.5-10%), with the majority showing mixed behavioral selectivity (Figure 5Bi)[57-59]. In
292 experimental mice, during male interactions the fraction of sniff-selective units was reduced by
293 ~40% relative to controls (3.9 □ 2% in OARs gRNAs mice vs. 8.9 □ 3% in Scr gRNAs mice) while
294 the proportion of attack-selective units was reduced by ~70% (1.8 □ 0.7% vs. 6 □ 0.9%; Figure 5B,
295 Di). The fraction of neurons exhibiting mixed selectivity (i.e., active during both behaviors) was
296 moderately reduced (~22%; Figure 5Di). Overall, there was an ~38% reduction in the fraction of
297 active (≥ 2σ above baseline) units during all male-directed behaviors (from 36.2% in control to
298 22.4% in experimental mice). In contrast, the fraction of female-directed sniffing- or mount-
299 selective units was similar between control and experimental males (Figure 5Dii).
300 As an alternative metric of a cell's behavioral tuning, we calculated its choice probability
301 (CP): a cell was considered "tuned" to one of two pairwise-compared behaviors if it exhibited a
302 CP > 0.7 that was significantly different ($p < 0.5$) from shuffled data[59]. We observed an ∼80%
303 and ∼70% reduction in the percentage of attack- and sniff-tuned units, respectively, in
304 experimental vs. control mice during male-male interactions (Figure 5Ei), with a concomitant
305 ∼18% increase in the fraction of units exhibiting mixed selectivity (CP for sniff vs. attack ≤ 0.7;
306 Figure 5Ei, gray bars and Supplementary Figure S5D). In contrast, the percentage of units tuned
307 to sniffing females (vs. sniffing males) was increased in experimental mice (28.8 □ 3% vs. 41.1 □
308 3%; Figure 5Eiii). We also observed a slight increase in the fraction of sniff female (vs. mount
309 female) -tuned units and mount female (vs. attack male) -tuned units in experimental vs. control
310 animals (Figure 5Eii). This analysis suggests that perturbation of normal OXTR/AVPR1a-

311 mediated signaling decreases the relative number of units tuned to specific male-directed behaviors
312 and increases the fraction of cells tuned for female-directed behaviors.

313 Despite these quantitative changes in behavior-selective tuning, there was no significant
314 difference between control and experimental mice in the performance of linear decoders trained to
315 identify and distinguish attack from sniffing behavior based on the activity of VMHvl^{Esr1} units
316 (Supplemental Figure S5E). Decoders trained on data from each group were able to accurately
317 distinguish these behaviors in held out testing data with close to 100% accuracy. Thus, the
318 population coding of social behavior by VMHvl^{Esr1} neurons[59] is not affected by co-disruption of
319 *Oxtr/Avpr1a.*

320

321 **VMHvl^{Esr1} line attractor dynamics require Oxtr/Avpr1a-mediated signaling**

322 In addition to the level of activity and feature-specific tuning, neural dynamics can play an
323 important role in the neural coding of cognitive function or internal state[17]. Using unsupervised
324 linear dynamical systems modeling[63], we recently discovered an approximate line attractor in
325 VMHvl neural state space that encodes a low-dimensional, scalable representation of
326 aggressiveness [20]. This line attractor is implemented by a subset of VMHvl^{Esr1} neurons (~20-25%)
327 whose collective activity ramps up as social interactions escalate to attack and thereafter decays
328 with a long (~100s) time constant[20]. This long time constant reflects persistent activity in this
329 subset. Since neuromodulatory signaling has been implicated in some forms of persistent neural
330 activity[27,82,83], we investigated whether line attractor dynamics during aggression are altered when
331 OXTR/AVPR1a-mediated signaling is perturbed.

332 We fit a recurrent switching linear dynamic system (rSLDs) model[84] using data from
333 animals with at least 31 imaged units, thereby reducing the dimensionality of the data to 5 latent

334 factors and three states (S1-S3) which captured ~85% of the observed variance in neural activity.
335 Attack behavior occurred during a single rSLDs state in both control and experimental males. In
336 control mice, the time constant (τ) of the 1st rSLDS dimension (derived from the first Eigenvalue
337 of the fit dynamics matrix; see Methods) was much higher than that of the 2nd dimension (~100-
338 120s vs. ~40s; Figure 6A). This yielded a line attractor score (calculated as the $\log_2$ of the ratio of
339 the τ 's of the 1st and 2nd dimensions) of ~1.5 (Figure 6F), similar to that observed in mice without
340 CRISPR/Cas9 gene editing[20]. In contrast, in experimental mice the first two rSLDS dimensions
341 had statistically indistinguishable τ values (<50s; Figure 6C), due to a reduced 1st dimension τ
342 (Supplementary Figure 6D) and consequently a line attractor score close to zero (Figure 6F).
343 To visualize these dynamics in neural state space, we generated 2D flow field graphs
344 spanned by the first two PCs of the fit rSLDS model. The flow fields are comprised of arrows that
345 indicate the rate and direction of change in neural population activity at different points in state
346 space during social interactions (Supplementary Figure S6C). The 2D flow field of control mice
347 (Scr gRNAs) revealed a roughly linear region of low vector flow constituting the line attractor,
348 along which the neural population vector progressed during an inter-male interaction (Figure 6G
349 and Supplemental Figure S6C, dashed black lines). In a 3D dynamic landscape, where the length
350 of the flow-field vectors at each position in neural state space is converted into the height of the
351 landscape (and represented as a heat scale), in control animals neural activity progressed slowly
352 along a trough-like structure (the line attractor) as aggression escalated (Supplementary Figure
353 S6Hi). In contrast, in experimental mice (OARs gRNAs) this line attractor was absent and was
354 replaced by a point attractor (appearing as a white circle in 2D and a cone in 3D), from which the
355 population activity vector made transient excursions during bouts of sniffing or attack (Figure 6G,
356 H and Supplemental Figure S6Cii). This point attractor is a "trivial" fixed point, corresponding to

357 the resting state of a system in which activity decays to baseline in the absence of inputs. These
358 data indicate that Oxtr/Avpr1a-mediated signaling is required for the emergence of line attractor
359 dynamics in VMHvl during aggression.

360 To investigate in more detail how co-disruption of *Oxtr/Avpr1a* perturbs VMHvl^{Esr1}
361 attractor dynamics, we projected the weighted average of neuronal activity in the 1st rSLDS
362 dimension (which generates the line attractor) onto the time axis and overlayed behavior
363 annotations. As reported previously[20], in control mice this activity ramped up during the
364 progression from male-directed sniffing to attack, eventually reaching a plateau where it decayed
365 slowly between attack bouts towards a single intruder and remained elevated between sequential
366 trials with different intruders (Figure 6B, Ei and Supplementary Figure S6A, "post intruder"). In
367 contrast, in experimental mice activity in the 1st dimension decayed rapidly in between attack
368 bouts, displaying a "sawtooth" profile, and was significantly lower during the post-intruder (i.e.,
369 inter-trial) interval (Figure 6D, Eii and Supplementary Figure S6B). The observation that 1st
370 dimension activity in experimental mice is transiently elevated during aggressive episodes, but
371 does not remain stable across attack bouts and trials, indicates that these neurons are still active
372 during attack, but do not integrate recent experiences in the same way as normal mice.

373

374 **Oxtr/Avp1ra-mediating signaling controls VMHvl ^{Esr1} persistent neural activity**

375 We next asked whether changes in the dynamics of VMHvl^{Esr1} neurons caused by co-
376 disruption of *Oxtr/Avpr1a* could account for the elimination of the line attractor in experimental
377 mice. We focused initially on cells that were strongly weighted by the 1st rSLDS dimension (stem
378 plots in Figure 7Aiii). In raster plots from control mice, these units exhibited activity that persisted
379 across inter-attack bout intervals and decayed slowly after removing the intruder male, visible as

380 a “smearing” of rasters over time (Figure 7Ai, Scr gRNAs). In contrast, analogous units from
381 experimental mice exhibited activity time-locked to attack bouts, visible as a vertical stripe-like
382 pattern (Figure 7Ai, OAR gRNAs). To quantify these dynamics, we computed the average
383 autocorrelation half-width (ACHW)[59], an approximate measure of the decay constant[85,86], for each
384 1st dimension-weighted unit. The mean ACHWs during the first minute of interaction were
385 significantly shorter in experimental (9.86 □ 1 s) than in control mice (28.6 □ 1.23 s), by ~20
386 seconds (Figure 7Aii, inset).

387 A reduction in the average ACHW was also observed in the VMHvl^{Esr1} population as a
388 whole (Figure 7B), although the group difference between means (50.9%) was smaller than that
389 calculated for 1st dimension-weighted units (65.4%). In contrast, the mean and cumulative
390 distribution of ACHWs were only slightly reduced (~by 22%) during male-female interactions
391 (Figure 7Ci-ii). Thus, the dynamics of individual VMHvl^{Esr1} units are faster, on average, in
392 experimental than in control mice during male-male social interactions. This reduction in ACHWs
393 is consistent with and may explain, the loss of line attractor dynamics caused by co-disruption of
394 *Oxtr/Avpr1a*.

395

396 **OXT and AVP evoke persistent responses in VMHvl^{Esr1} neurons *ex vivo***

397 The observation that co-disruption of *Oxtr/Avpr1a* shortened the average decay time of
398 Esr1^{+} units raised the question of whether adding these peptides to VMHvl would, conversely
399 lengthen this decay. Because it is not technically feasible to apply drugs or peptides directly at the
400 site of miniscope imaging, we utilized the *ex vivo* VMH brain slice preparation (Figure 1F). We
401 transiently perfused the slices with a cocktail of OXT & AVP, imaged activity at single cell
402 resolution, and fit a dynamical systems model to the data using rSLDs (Supplementary Figure

403 S7G). Although this fit model was based on only two dimensions (x1, x2), it captured 85% of the
404 observed variance in neural activity. The time constant of dimension x1 (~90s) was ~8-9 -fold
405 greater than that of x2 (~15s; Supplemental Figure S7H), similar as what we observed *in vivo*
406 (Figure 6A, C). This suggested the existence of two populations of VMHvl^{Esr1} neurons that respond
407 to the neuropeptides with distinct neural dynamics. Indeed, stem plots revealed that the neurons
408 highly weighted by dimension x1 were distinct from those weighted by x2 (Supplementary Figure
409 S7I). Plotting the time-varying average activity of the neurons contributing to these two
410 dimensions revealed that x1 neurons exhibited slowly decaying responses to OXT+AVP
411 application, while x2 neurons exhibited more transient responses (Supplementary Figure S7J-N).
412 These data indicate that acute application of OXT and AVP can evoke persistent responses in a
413 subset of VMHvl^{Esr1} neurons *ex vivo*.
414
415 **DISCUSSION**
416 CRISPR/Cas9 gene editing technology[48,87] has revolutionized virtually every area of
417 biology, but has thus far had relatively little impact on Systems Neuroscience. Using a novel
418 approach that integrates such gene editing[48,87] with population imaging[49] and dynamical systems
419 analysis[63], we show here that OXT and/or AVP receptors are required for persistent neural activity,
420 line attractor dynamics and aggression in VMHvl^{Esr1} neurons that control social behaviors [54,55,56,58].
421 More generally, these results demonstrate an important role for peptidergic signaling in
422 population-level slow neural dynamics and attractor formation, and suggest that neuropeptides
423 may control certain behaviors, at least in part, through an influence on such emergent properties.
424 The CRISPRoscopy approach developed here may be generally useful for unifying molecular and

425 circuit-level approaches with "manifold"-level approaches[13,14] to understand the neural control of
426 behavior, emotion and cognition[22].

427 **Methodological considerations**

428 We implemented several technical innovations to combine CRISPR/Cas9-mediated gene
429 editing with calcium imaging in a cell type-specific, anatomically restricted manner. We generated
430 a series of viral vectors, which are distinct from earlier constitutive[88] or conditional[89] constructs,
431 to integrate Cre-dependent gene editing with calcium imaging. Our conditional expression system
432 avoids reliance on Cre-dependent chromosomally integrated Cas9 transgenes[90], eliminating time-
433 consuming and cumbersome genetic crosses, and better aligns GCaMP and Cas9 expression in
434 adult mice, bypassing transient developmental expression of Cre drivers. We also harnessed the
435 multiplex gene editing capabilities afforded by CRISPR/Cas9 to target up to four different genetic
436 loci using a single viral construct. Finally, our system permits the flexible combination of different
437 genetic perturbations with different reporters of neuronal activity or signaling.

438 **The effects of Oxtr/Avpr1a co-disruption on VMHvl^{Esr1} neuronal activity and behavioral**
439 **tuning**

440 In principle, the observed reduction in aggressive behavior could be a consequence of a
441 reduction in the activity or attack-specific tuning of VMHvl^{Esr1} neurons. We analyzed the level of
442 activity of these neurons in mice with co-disruption of *Oxtr* and *Avpr1a* using fiber photometry
443 ("CRISPRometry") and miniscope imaging ("CRISPRoscopy"). A significant reduction in bulk
444 VMHvl^{Esr1} neural activity during attack and sniff episodes was observed in mice with bilateral co-
445 disruption of *Oxtr/Avpr1a.* However, because this manipulation also reduced aggression, those
446 results did not distinguish whether the decreased bulk calcium signal is a cause or consequence of
447 this behavioral phenotype. Unilateral CRISPRoscopy (which does not cause any reduction in

448 aggressive behavior) revealed a small but statistically significant decrease in average unit activity
449 during sniffing or attacking males. This subtle decrease seems unlikely to account for the decreased
450 aggressiveness seen in mice with bilateral gene disruptions, although it formally cannot be
451 excluded.

452 Previous studies from our laboratory have reported that the percentage of VMHvl^{Esr1}
453 neurons specifically tuned to attack behavior is relatively small, from 2.5-10% [57-59]. In mice with
454 co-disruption of *Oxtr* and *Avpr1a*, the percentage of attack- and sniff-selective cells was reduced.
455 This result was confirmed by choice-probability analysis[59] which also revealed an increase in the
456 proportion of cells displaying "mixed selectivity" (i.e., tuned to both sniffing and attack). Whether
457 a relatively large reduction in the small fraction of attack-tuned neurons in VMHvl can account
458 for the behavioral phenotype is not yet clear, especially if some of those cells are converted to
459 mixed-selectivity neurons, rather than simply inactivated. Previous studies have shown that attack
460 behavior can be accurately decoded from VMHvl^{Esr1} population activity despite the dearth of
461 attack-tuned cells[59], and we show here that the performance of such decoders was not affected by
462 co-disruption of *Oxtr/Avpr1a*.

463 **The impact of Oxtr/Avpr1a co-disruption on neural dynamics**

464 More striking physiological phenotypes were observed in experimental mice when we
465 examined the dynamics of VMHvl^{Esr1} neuronal activity. In control mice many of these neurons
466 exhibited persistent activity, with autocorrelation half-widths (ACHWs; an approximation of the
467 neuronal time constant) ranging over tens of seconds. Co-disruption of *Oxtr/Avpr1a* caused a
468 strong and highly statistically significant reduction in the average ACHW of VMHvl^{Esr1} neurons.
469 These data reveal a requirement for normal OXTR/AVPR1a-mediated signaling in persistent
470 neural activity at the population level. Our between-subject comparisons do not allow us to

471 distinguish whether co-disruption of *Oxtr/Avpr1a* reduced the population average time constant
472 by changing the dynamics of individual cells, or simply by reducing the proportion of active cells
473 with fixed, slow dynamics. However, bath application of OXT+AVP induced persistent calcium
474 responses in a subset of VMHvl^{Esr1} neurons *ex vivo* (Supplemental Figure S7). Interestingly,
475 persistent activity in entorhinal cortical neurons has previously been shown to require muscarinic
476 cholinergic signaling *ex vivo*[82], and is thought to underlie some forms of working memory[83,91].
477 Consistent with these changes in single unit dynamics, fitting a linear dynamical systems
478 model[63] to the CRISPRoscopy data revealed a large decrease in the time constant of the 1st rSLDS
479 dimension. Accordingly, the average time-varying activity of these neurons did not show
480 persistence during aggression, but rather exhibited a "saw-tooth"-like pattern time-locked to
481 individual attack bouts. In addition, persistent activity between aggression trials[20] was severely
482 reduced. Most strikingly, in 2D and 3D projections of the rSLDS manifold the line attractor[20] was
483 absent and replaced by a point attractor centered on the resting state (Figure 6F, G).
484 A parsimonious hypothesis is that the reduction in single-unit persistent activity caused by
485 co-disruption of *Oxtr/Avpr1a* is responsible for the loss of line attractor dynamics. These changes
486 in dynamics may in turn be responsible for the reduction in aggressive behavior that is caused by
487 the same perturbation. However, a contribution from the small but significant reductions observed
488 in the number, activity and tuning specificity of attack-selective neurons cannot be excluded.
489
490 **A line attractor dependent on neuropeptide signaling**
491 The data presented here provide to our knowledge the first evidence in any system of a
492 requisite role for neuropeptide signaling in line attractor dynamics. In contrast, most theoretical
493 studies of attractor dynamics to date have assumed that they reflect recurrent fast synaptic

494 connectivity[17,92], although that has been experimentally demonstrated so far only in the *Drosophila*
495 ring attractor system[23,28]. The finding that neuropeptide signaling is required *in vivo* for persistent
496 activity and line attractor dynamics in VMHvl is consistent with recent slice recording studies
497 reporting sparse local fast glutamatergic connectivity and predominantly neuropeptidergic
498 transmission in this nucleus[93]. Nevertheless, the two mechanisms are not mutually exclusive.
499 Indeed, in an earlier study we generated recurrent network models of persistent activity displayed
500 by VMHdm^{SF1} neurons that mediate defensive behaviors[94-96], and found that only models in which
501 local transmission occurred on a time scale consistent with slow neuromodulatory signaling were
502 consistent with our observational data[11].

503 The finding that a line attractor which represents an internal motive state of
504 aggressiveness[20] is dependent on neuropeptidergic signaling is important for several reasons. First,
505 neuropeptide gene expression is strongly modulated by physiological influences including
506 hormones[97] and neural activity[98]. Through this mechanism, such influences may mediate
507 physiological state-dependent changes in attractor dynamics[19]. Second, neuropeptide receptor
508 expression is more restricted than the expression of receptors for biogenic amines[99], another
509 important class of neuromodulators. This specificity could allow the regulation of different (and
510 potentially competing) attractors within the same network by distinct neuropeptides, depending on
511 differential receptor expression; VMH neurons collectively express dozens of neuropeptides and
512 close to 100 GPCRs[69,100]. Finally, neuropeptides such as CRH[101] and NkB[30,102] are known to
513 mediate responses to psychological stressors, which are known etiological factors in some
514 neuropsychiatric disorders. It has been proposed that these disorders may reflect changes in
515 attractor dynamics in certain brain regions[103]. Our data suggest that such changes could potentially

516 result from stress-induced alterations in neuropeptide signaling[104,105] that is necessary for attractor
517 formation.

518 The results described here constitute a "first-in-class" experiment that demonstrates, on the
519 one hand, how the power of multiplex gene editing technology[48,87] can combined with single cell
520 imaging to link emergent properties discovered by dynamical systems analysis to underlying
521 molecular control mechanisms[17]. On the other hand, they open a new window onto systems-level
522 mechanisms that may mediate the behavioral functions of some neuropeptides[39,41]. In this way,
523 this work may help to enable mechanistic explanations in neuroscience that unify different levels
524 of abstraction and of biological organization[22].

525 **Limitations**

526 A technical limitation of our approach is that two different viruses are used to deliver
527 gRNAs-GCaMP and Cas9. Consequently, not all GCaMP^{+} cells captured in our imaging analysis
528 are necessarily Cas9^{+} (and therefore mutant for *Oxtr/Avpr1*). Our data indicate co-infection rates
529 of ~65-80% depending on the viruses used. Developing single-vector approaches[106] would ensure
530 that calcium imaging is restricted to cells that co-express both Cas9 and gRNAs. Another limitation
531 is that we lack an accurate estimation of the fraction of cells exhibiting homozygous INDELs in
532 the *Oxtr* and *Avpr1a* loci *in vivo*. Consequently, our results may underestimate the magnitude and
533 penetrance of the effects of a complete null mutation of *Oxtr/Avpr1a* in all VMHvl^{Esr1} neurons.
534 Another limitation is that our statistics are based on between-subject comparisons of experimental
535 vs. control mice, necessitating large sample sizes for behavioral experiments. Statistical power
536 could be increased by using an inducible CRISPR/Cas9 system permitting within-subject
537 comparisons, which would also clarify the interpretation of the underlying mechanism. Finally,
538 our results do not distinguish the respective roles of OXTR and AVPR1a, nor do they establish the

539 cellular source and identity of the endogenous peptide(s) release that activates these receptors *in*
540 *vivo* during aggression. Further studies will be required to elucidate these biologically important
541 details.
542

543 **ACKNOWLEDGEMENTS**

544 We thank H. Inagaki, A. Kennedy, B. Weissbourd, M. Schnitzer and S. Linderman for critical
545 feedback on this manuscript, C. Chiu for laboratory management, G. Mancuso and L. Chavarria
546 for administrative assistance, and members of the Anderson lab for helpful comments on this
547 project. G.M. has been supported by post-doctoral fellowships from the Tianqio and Chrissy Chen
548 Institute for Neuroscience, the Helen Hay Whitney Foundation and the Della Martin Foundation.
549 A. N. is supported by a National Science Scholarship from the Agency of Science, Technology
550 and Research, Singapore. This work was supported in part
551 by NIH grants NS123916, MH1223612, and MH070053 . D.J.A. is an Investigator of the Howard
552 Hughes Medical Institute. The content of this paper is solely the responsibility of the authors and
553 does not necessarily represent the official views of the National Institutes of Health. We support
554 inclusive, diverse, and equitable conduct of research. We acknowledge that this research was
555 conducted at Caltech, which is located on the unceded land of the Indigenous Tongva people.

556 **Author contributions**

557 G.M and D.J.A conceived the project. G.M and D.J.A. wrote and prepared the manuscript, with
558 input and help from A.N. G.M performed all the experiments, with the occasional help from B.Y
559 for the miniscope imaging and D.K. for the two-photon slice imaging. G.M and A.N performed

560 quantitative measurements of behavior and microendoscope imaging data. A.N performed the
561 dynamical system modeling and decoder analyses.

562

563

564

565

566

567

568 **MAIN FIGURE LEGENDS**

569 **Figure 1. VMHvl^{Esr1} neurons co-express Oxytocin and Vasopressin receptors and respond to**
570 **these peptides *ex vivo***

571 **A)** A graphic illustration of the resident intruder behavioral assay used in this study (top). A
572 graphic illustration of male- (red), female-(green), and mixed-selective (grey) VMHvl^{Esr1}
573 responses in male residents during interactions with male vs. female intruders. Optogenetic
574 interrogation of VMHvl^{Esr1} cells in male mice controls appetitive (sniffing) and consummatory
575 (mount and attack) behaviors towards conspecific intruders. **B)** Violin plots illustrating the
576 expression of *Esr1, Avpr1a* and *Oxtr* mRNAs in single cell gene clusters (top-colored boxes);
577 "max CPM", maximum counts per million reads. Green, blue, and red boxes highlight the
578 expression of *Esr1, Avp1ra,* and *Oxtr* in the three major VMHvl gene clusters. **C)** t-SNE plots
579 illustrating the distribution of *avpr1a* and *oxtr* mRNAs (ii) in single cells from the VMH. All cells
580 visible in the inset are Esr1^{+} (see Supplemental Figure S1C). **D)** Example of ~50 individual VMH
581 cells co-expressing *Esr1, Avpr1a,* and *Oxtr* mRNAs. **E)** Venn diagram of *esr1, avpr1a,* and *oxtr*
582 mRNA expressing neurons within the VMHvl. The size of each circle is proportional to the number

583 of neurons. Numbers represent individual neurons expressing each receptor gene. Analyses in (B-
584 E) are based on data originally reported in Kim et al. (2019). **F)** Graphic illustration of the two-
585 photon *ex vivo* calcium imaging experiments. (i) Acute brain slices from male ESR1-2A-CRE
586 animals that express Cre-dependent GCaMP7f virus were perfused with OXT and/or AVP
587 neuropeptides. (ii) Quantification of GCaMP7f calcium responses in $Esr1^{+}$ cells to a 400nM
588 cocktail of AVP/OXT (n=124 cells, 4=mice). Gray rectangle depicts the duration of the bath
589 application of peptides. For responses to individual peptides see Supplemental Figure S1F.
590 Statistics: Values plotted as mean ± S.E.M. ****$p<0.0001$ Mann-Whitney test
591

592 **Figure 2. CRISPR/Cas9 based co-perturbation of *Oxtr* and *Avpr1a* reduces territorial**
593 **aggression in males.**

594 **A)** A schematic of the strategy for region-restricted multiplex CRISPR/Cas9 gene editing *in vivo*.
595 A mixture of the two viruses was used- A Lentivirus (LV) constitutively expressing four different
596 gRNAs and the red fluorescence marker DsRed (i). A Adenovirus (AAV) constitutively expressing
597 the Cas9 protein (See Methods) (ii). Male residents were injected bilaterally in the VMH with the
598 OARs-Cas9 (experimental group) or Scr-Cas9 (control group) viral mixture. **B)** Two different
599 gRNAs target each GPCR receptor gene. Scrambled gRNA sequences were used as negative
600 controls. **C)** Immunostaining against the DsRED (red) and Cas9 (green) proteins in coronal
601 hypothalamic sections from animals co-injected with LV gRNA virus and the Cas9 AAV. Sections
602 are counterstained with Dapi (blue). **D)** Quantification of Cas9+ cells (Aii) infected with the gRNA
603 (Ai) virus in the hypothalamus. n= 3 mice. **E)** Diagram of the behavioral paradigm used for testing
604 the effects of Oxtr and Avpr1a mediated signaling in social behaviors. **F)** Quantification of the
605 number (i) and the total time spent attacking (ii), or sniffing (iii) male intruders in experimental

606 and control mice. **G)** Quantification of the number (i) and the total time spent mounting (ii) or
607 sniffing (iii) female intruders in experimental and control mice. n= 11 mice per group. Statistics:
608 Mann-Whitney test was performed **p≤0.01.
609

610 **Figure 3. Co-perturbation of OXT/AVP signaling alters VMHvl^{Esr1} bulk calcium activity**

611 **A)** A schematic of the strategy for cell type specific Cre-dependent multiplex CRISPR/Cas9 gene
612 editing and calcium imaging *in vivo*. As before, two different gRNAs target each GPCR receptor
613 gene. Scrambled gRNA sequences were used as negative controls. Cre-dependent expression of
614 GCaMP8s (i) and Cas9 proteins (See Methods) (ii). **B)** Graphic illustration of unilateral fiber
615 photometry recording experiments in ESR1- 2A-CRE male residents that are bilaterally co-
616 injected with Cre-dependent Cas9 AAV and a Cre-dependent OARs-GCaMP8s gRNA
617 (experimental group) or Scr-GCaMP8s gRNA AAVs (control group) in the VMHvl. Coronal
618 histology section showing the expression of GCaMP8s (green) in VMHvl. Section counterstained
619 with Dapi (blue). **C)** Quantification of the number (i) and the total time spent attacking (ii) or
620 sniffing (iii) male intruders in experimental and control mice. n=16 control and n=13 experimental
621 mice. **D)** Quantification of the number (i) and the total time spent mounting (ii) or sniffing (iii)
622 female intruders in experimental and control mice. n=16 control and n=13 experimental mice. **E)**
623 Examples of fiber photometry traces from a control and experimental mouse during male-directed
624 sniffing. **F)** Z-scored behavioral triggered average (BTA) of VMHvl^{Esr1} activity (i), the average
625 area under the curve (AUC) (ii) and the peak PETH signal during male-directed sniffing (1 min).
626 Each dot represents a bout. n=5 mice per group. **G)** Examples of fiber photometry traces from a
627 control and experimental mouse during attack. **H)** Z-scored BTA of VMHvl^{Esr1} activity (i), the

628 average area under the curve (AUC) (ii) and peak PETH signal during attack. n=5 per group.
629 Statistics: Values plotted as mean ± S.E.M. Mann-Whitney test was performed *p≤0.05 **p≤0.01;

630

631 **Figure 4. Single cell "CRISPRscope" imaging of VMHvl^{Esr1} neurons with co-disruption of**
632 ***Oxtr/Avpr1a***

633 **A)** A graphic illustration of "CRISPRoscopy." Male ESR1-2A-CRE residents unilaterally co-
634 injected with a Cre-dependent Cas9 AAV and Cre-dependent OARs-GCaMP8s AAV
635 (experimental group) or Cre-dependent Scr-GCaMP8s AAV (control group) in the VMHvl (top).
636 Coronal histology section showing the expression of GCaMP8s (green) in VMHvl (bottom).
637 Section counterstained with Dapi (blue). **B**) Example of micro-endoscope single unit z-scored
638 responses towards female or male intruders from control (i) and experimental (ii) male residents.
639 **C)** Example of VMHvl^{Esr1} ensemble representations of intruder sex, for a control (i) and
640 experimental (ii) male, projected onto the first two axes of a PLS regression against intruder sex.
641 Traces are colored by intruder sex identity. The percentage of variance explained by the first two
642 PLS components is noted for each mouse. **D**) Accuracy of frame-wise decoders predicting the sex
643 of the intruder trained on VMHvl^{Esr1}neural activity in control and experimental animals. **E**)
644 Average single VMHvl^{Esr1}unit (σ) responses and **F)** cumulative distribution of VMHvl^{Esr1} activity
645 (σ) relative to pre-intruder baseline, towards male (i) or female (ii) intruders in control and
646 experimental mice during 1 minute of interaction. **G)** Percentage of male- or female selective, - or
647 co-active VMHvl^{Esr1} units (≥ 2σ above the pre-intruder baseline) in control and experimental mice.
648 n=5 control, n=7 Oxtr/Avp1ra targeted animals. Statistics: Values plotted as means with ± S.E.M
649 in (F) and in (G). Nested Mann-Whitney test was performed except (F), where nested
650 Kolmogorov–Smirnov test was used. **p≤0.01 ***p≤0.001 ****p≤0.0001

651

652 **Figure 5. Social behavior-selective activity and tuning of VMHvl^{Esr1} neurons with co-**
653 **disruption of *Oxtr*/*Avpr1a***

654 **A)** Cumulative distribution of VMHvl^{Esr1}activity (σ) during male- (sniffing and attack) or female
655 (sniffing and mounting) -directed behaviors in control and experimental mice relative to the pre-
656 intruder baseline. **B**) Scatter plots of single VMHvl^{Esr1} unit activity (σ) during male-directed
657 sniffing or attack in control and experimental mice. Green data points depict units with ≥
658 2σ activity during male-directed sniffing and < 2σ activity during attack, relative to the pre intruder
659 baseline activity. Red data points depict units with ≥ 2 activity during attack and < 2σ activity
660 male-directed sniffing, relative to the pre intruder baseline activity. **C)** Average activity (σ) of
661 single VMHvl^{Esr1} units during male-(sniffing and attack) or female (sniffing and mounting)-
662 directed behaviors in control and experimental mice relative to the pre- intruder baseline. **D**)
663 Percentage of VMHvl^{Esr1} units active (defined as ≥ 2σ relative to pre intruder baseline) during
664 male- (i) or female-directed behaviors (ii) in control and experimental mice. **E**) Choice probability
665 histograms of VMHvl^{Esr1} tuning during male- and female-directed behaviors in control and
666 experimental mice. Statistics: Values plotted as means in (A) (± S.E.M), (D) and (E). Nested
667 Kolmogorov–Smirnov test was used in (A), whereas the Nested Mann-Whitney test was performed
668 in (C). **p≤0.01 ***p≤0.001 ****p≤0.0001

669

670 **Figure 6. VMHvl^{Esr1} line attractor dynamics require Oxtr/Avpr1a-mediated signaling**

671 **A)** Average time constant (τ) of all dimensions, arranged in decreasing order in control mice. **B)**
672 Normalized activity projection onto the time axis of the longest time constant (integration
673 dimension) for VMHvl^{Esr1} units in control mouse M1. **C)** Average time constant of all dimensions,

674 arranged in decreasing order for VMHvl^{Esr1} units in experimental mice. **D)** Normalized activity
675 projection onto the time axis of the 1st dimension (no integration) for VMHvl^{Esr1} units in
676 experimental mouse M1. **E)** Mean normalized VMHvl^{Esr1} activity of the 1st dimension during all
677 behavioral bouts and after removing the intruder male (post-intruder) in control (i) and
678 experimental (ii) mice. **F)** Line attractor score for VMHvl^{Esr} population activity in control and
679 experimental mice. n = 4 control and n =7 in experimental group.**G)** Neural state space with the
680 trajectories projected over time within the inferred flow field rSLDS states for VMHvl^{Esr1} in
681 control (i) and experimental (ii) mouse. **H)** Inferred 3D dynamic landscape in VMHvl control
682 mouse M1(i) and experimental mouse M1(ii). Different views of line (i) and point attractors (ii)
683 are shown. Red arrows depict the neural trajectory associated with attack. 1 minute of sniffing
684 behavior following the introduction of an intruder male is displayed in the behavioral raster plots
685 in (B) and (D). Statistics: Kruskal-Wallis test was performed in (A) and (C). Paired t-test was
686 performed inin (E) and Mann-Whitney test in (F) *$p \leq 0.05$ **$p \leq 0.01$
687
688 **Figure 7. Oxtr/Avp1ra-mediating signaling controls VMHvl ^{Esr1} persistent neural activity**
689 **A)** Behavioral raster plot and the corresponding neural activity (z-score) of individual VMHvl^{Esr1}
690 units that contribute to the 1st dimension in control (left) and experimental (right) mouse (i).
691 Cumulative distribution and inset box plot of VMHvl^{Esr1} persistence, measured by autocorrelation
692 half width (ACHW) (ii) of units identified in the stem plots (iii) from control (n=4) and
693 experimental (n=7) mice. The whiskers in the inset box plot represent the minimum and maximum
694 values. **B)** Average single unit (i) and cumulative distribution (ii) of neuronal persistence measured
695 by ACHW of all VMHvl^{Esr1} recorded units in control and experimental mice during male-male,
696 and **C)** during male-female interactions. n=5 control, n=7 experimental animals. **D)** A graphic

697 illustration depicting our working model. Oxtr and Avpr1a-mediated signaling control aggression
698 escalation by regulating VMHvl^{Esr1} persistent activity and line attractor dynamics (left) during
699 male-male interactions. However, co-perturbation of *Oxtr* and *Avpr1a* results in a severe reduction
700 of the slow neural dynamics of VMHvl^{Esr1} neurons and the emergence of a trivial point attractor.
701 Under such conditions, male animals fail to display a high level of offensive aggression against
702 male conspecifics (right). Statistics: Values plotted as mean ± S.E.M. Nested Mann-Whitney test
703 was performed for (Bi, Ci, Aii inset). Kolmogorov test was performed (Aii, Bii, Cii) *$p \leq 0.05$
704 **$p \leq 0.01$ ****$p \leq 0.0001$
705
706
707 **SUPPLEMENTAL FIGURE LEGENDS**

708 **Figure S1. Expression and *ex-vivo* functional characterization of *Oxtr* and *Avpr1a* in the**
709 **VMH, related to Figure 1**

710 **A)** A diagram portraying the diverse methodologies employed to investigate the role of
711 neuromodulators in the mammalian brain. Among the most recent predominant strategies are the
712 systemic administration of agonists/antagonists targeting G-protein-coupled receptors (GPCRs)[107]
713 or the use of knock-out animals combined with *in vivo* single recording unit approaches[108].
714 However, there is a requirement for novel regionally restricted gene-editing strategies, with cell
715 type specificity[109], compatible with bulk[88,110,111] or single-cell calcium recording methods[90,112]
716 from many cells in freely moving animals (Mountoufaris et al). **B)** Violin plots illustrating the
717 expression of *esr1, avpr1a,* and *oxtr* mRNAs outside the VMH and in non-neuronal clusters; "max
718 CPM", maximum counts per million reads. **C)** t-SNE plots illustrating the distribution of *esr1* (i)
719 or *avpr1a* and *oxtr* mRNAs (ii; from Figure 1C) in single cells from the VMH. "FPKM", fragments

720 per kilobase of exon per million mapped fragments. **D)** Violin plots illustrating the expression of
721 *Esr1, Oxt,* and *Avp* mRNAs in VMHvl; "max CPM", maximum counts per million reads. **E)** Venn
722 diagram of *esr1, avpr1a,* and *oxtr* mRNA expressing neurons in the ventral part of the VMH and
723 the surrounding areas. **F)** Quantification of $Esr1^+$ responses to 400nM of Avp (n=62 cells from 3
724 mice) or OXT (n=79 cells from 3 mice). n=70 cells not activated in brain slices from 3 mice. The
725 shadow area depicts the duration of the bath application of peptides. **G**) An example field of view
726 of spontaneous active (left) and induced $Esr1^+$ GCaMP7f calcium responses to 400nM OXT &
727 AVP. Statistics: Nested Mann-Whitney test was performed, and values were plotted as mean ±
728 S.E.M. in (D). ****$p \leq 0.0001$
729
730 **Figure S2. Experimental validation and behavioral characterization of CRISPR/Cas9 based**
731 ***Oxtr* and *Avpr1a* perturbations, related to Figure 2**
732 **A)** T7E1-endonuclease treated *Oxtr* (left) and *Avpr1a* (right) PCR products from N2a-Cas9
733 expressing cells, transfected with gRNAs against *Avpr1a or Oxtr*. As a negative control, scrambled
734 gRNAs (Scr) were used. Yellow stars indicate the cleavage products, indicating successfully
735 induced Cas9-mediated insertions or deletions (INDELs) in the coding sequence complementary
736 to the gRNAs. **B)** Quantification of the percentage of animals attacking (i), the average duration
737 of each attack bout (ii), the latency of the 1st attack bout (iii), and the interval between attack bouts
738 (iv) against a male intruder. n=11 mice per group. **C)** Quantification of the number and time-
739 varying probability of attack bouts against a male intruder (i-ii). n=11 mice per group.
740 Quantification of the average velocity during attack in control (n=9 mice) and experimental mice
741 (n=8 mice) (iii). **D)** Quantification of the percentage of animals mounting (i), the average duration
742 of each mounting bout (ii), the latency of the 1st mounting bout (iii), and the interval between

743 mounting bouts (iv) in control and experimental mice during male-female interactions. n=11 mice
744 per group. Statistics: nested Mann-Whitney test was performed, and values were plotted as mean
745 ± S.E.M. *p≤0.05. ****p≤0.0001.
746
747 **Figure S3. Effects of *Oxtr* and *Avpr1a* co-perturbation on male-, female-directed behaviors**
748 **and bulk calcium activity, related to Figure 3**
749 **A)** Immunostaining against the GCamp8s (green) and Cas9 (red) proteins in coronal hypothalamic
750 sections from ESR1-2A-CRE animals co-injected with a Cre-dependent Cas9 AAV and Cre-
751 dependent gRNA-Gcamp8s AAV. Sections counterstained with Dapi (blue). Arrows depict the
752 expression of Cas9 protein in GCamp8s Esr1 double-positive cells (i). Quantification of GCamp8s
753 positive cells expressing the Cas9 protein (ii). n= 3 mice. **B)** Quantification of the number of $Esr1^{+}$
754 neurons responding to 400nM of AVP and OXT in brain slices from ESR1-2A-CRE mice co-
755 injected with the Cas9 AAV and Cre-dependent OARs-GCaMP8s AAV (experimental group) or
756 Cre-dependent Scr-GCaMP8s AAV (control group) in the VMHvl (see Figure 3Ai). Data points
757 represent brain slices. n=2 Scr RNA (control) and n=3 OARs (targeted) mice. **C)** Quantification
758 of the percentage of animals attacking (i), the average duration of each attack bout (ii), the latency
759 of the first attack (iii), the interval between attack bouts (iv), the number and the time-varying
760 probability (iv-v) of attack bouts during male-male interactions. n=16 control and n=13
761 experimental mice. **D)** Quantification of the average duration of each mounting bout (i), the latency
762 of the first mount (ii) and the interval between mounting bouts (iii) during male-female
763 interactions. n=15 mice each group. **E)** Z-scored BTA of $VMHvl^{Esr1}$ activity (i) and the area under
764 the curve (ii) during female-oriented sniffing (1 min). n=4 control and n=5 experimental mice. **F)**
765 Z-scored BTA of $VMHvl^{Esr1}$ activity (i) and the area under the curve (ii) during mounting. n=3

control and n=4 experimental mice. Statistics: Mann-Whitney test was performed, and values were plotted as mean ± S.E.M. **p≤0.01. ****p≤0.0001.

Figure S4. Effect of Oxtr/Avpr1a co-editing on intruder sex-specific representations, single unit neural activity and tuning, related to Figure 4

A) VMHvl^{Esr1} ensemble representations of intruder sex, for control (i) and experimental (ii) mice, projected onto the first two axes of a PLS regression against intruder sex. Traces are colored by intruder sex identity. The percentage of variance explained by the first two PLS components is noted for each male resident. **B**) Quantification of the PLS1 variance explained (which accounts for intruder sex) in control and experimental mice. **C)** Cumulative distribution of z-scored activity of all VMHvl^{Esr1} units during 1 min interaction with male (i) or female (ii) intruders in control and experimental mice. **D)** Average single unit activity (σ) of male responses (≥ 2σ relative to the pre-intruder baseline) between control and experimental mice. **E)** Percentage of male- or female selective or co-active units (≥ 2σ relative to the pre-intruder baseline), per imaged control (i) or experimental (ii) mouse. n=5 control, n=7 experimental animals. Statistics: Values in (C) are plotted as mean ± S.E.M. Nested Mann-Whitney test was performed in (B) and (D), while nested Kolmogorov–Smirnov test was used in (C) **p≤0.01 ***p≤0.001

Figure S5. Effect of Oxtr/Avpr1a co-editing on male-, female-directed single unit activity and tuning, related to Figure 5

A) Scatter plot of the average single VMHvl^{Esr1} unit activity (z-score) during male (i) and female (ii) directed behaviors in control and experimental mice. **B)** Cumulative distribution of VMHvl^{Esr1} activity (z-score) during male-directed (sniffing and attack; i & ii) and female-directed behaviors

789 (sniffing and mounting; iii-iv) in control and experimental mice. **C)** Average z-scored VMHvl^{Esr1}
790 activity normalized to the pre-behavior bout period during male-directed sniffing (i), attack (ii),
791 female-directed sniffing (iii) and mounting (iv). **D)** Choice probabilities histograms of male-
792 directed behaviors (attack vs. sniffing) in control and experimental mice. Mixed-tuned units (blue)
793 and units tuned for other behaviors (yellow) are highlighted. **E)** Accuracy of frame-wise decoders
794 predicting attack vs sniffing (i) and attack vs no attack (ii) trained on VMHvl^{Esr1}neural activity in
795 control or experimental animals. Decoders were trained and tested on held out data from each
796 group separately. Statistics: Values plotted as mean ± S.E.M. in (B). Nested Kolmogorov–Smirnov
797 test was used in (B), whereas nested Mann-Whitney test was performed in (C) and (E). *$p \leq 0.05$
798 **$p \leq 0.01$ ****$p \leq 0.0001$
799
800 **Figure S6. VMHvl^{Esr1} line attractor dynamics require Oxtr/Avpr1a-mediated signaling,**
801 **related on Figure 6**
802 **A)** Normalized activity projection onto the time axis of the longest time constant (integration
803 dimension) for VMHvl^{Esr1} units in control and **B)** in experimental mice. **C)** Schematic illustrating
804 inferred dynamics shown as flow fields, with the line attractor illustrated by a black dashed line in
805 control (i) and the point attractor with a purple dashed circle in experimental mouse (ii). The
806 different rSLDS states (S1-S3) are depicted with different colors. **D)** Quantification of the average
807 time constant (τ) of the 1st dimension in control and experimental mice. n=4 control and n=7
808 mutant. 1 minute of sniffing behavior following the introduction of an intruder male is depicted in
809 the behavioral raster plots in (A) and (B). Statistics: Mann-Whitney test was performed in (D).
810
811

812 **Figure S7.**

813 **A)** rSLDs modeling of Esr1^{+} cells calcium responses to 400nM OXT & AVP. Acute brain slices
814 from male ESR1-2A-CRE animals that express Cre-dependent GCaMP7f were used. **B)** Average
815 time constant of the identified two dimensions (X_1, X_2), arranged in decreasing order for acute
816 brain slices. **C)** Absolute rSLDS weight of neurons contributing to X_1 (top) and X_2 (bottom)
817 dimensions sorted by choice probability values for activity during the OXT & AVP perfusion
818 window. **D)** Heat maps of OXT & AVP induced slow persistent X_1 (left) and **E)** transient X_2
819 responses (right) VMHvl^{Esr1} neurons. **F)** Projection of population activity onto the time axis of the
820 slow persistent X_1 and **G)** the transient X_2 dimensions. **H)** Overlay projection of population activity
821 onto the time axis of the slow persistent X_1 and the transient X_2 dimensions.

822

823 **STAR METHODS**

824 EXPERIMENTAL MODEL AND SUBJECT DETAILS

825 All procedures were performed in accordance with NIH guidelines and approved by the Institutional
826 Animal Care and Use Committee (IACUC) at the California Institute of Technology (Caltech). We
827 used *Esr1*$^{Cre/+}$ [55] and *Oxtr*$^{Cre/+}$ [113] transgenic mice. Animals were housed and maintained on a reverse
828 12 h light-dark cycle with food and water ad libitum. We used wild-type (WT) C57BL/6N male mice
829 (experimental), C57BL/6N female mice or BALB/c females (for sexual experience), and BALB/c
830 male mice (intruders) were obtained from Charles River (Burlington, MA). Behavior was tested
831 during the dark cycle.

832 **Viruses**

833 The following AAVs were used in this study, with injection titers as indicated. Viruses with a high
834 original titer were diluted with clean PBS on the day of use. AAV1-Syn-Flex-GCaMP7f (2.1 x e^{13})
835 was purchased from Addgene. AAVDJ/8-EFS-NC-SpCas9-HA -NLS-Poly(A) (pBK694) (2.00x
836 e^{13}) and AAV9-EFS-NC-SpCas9-HA -NLS-Poly(A) (2.17x e^{13}) purchased from Duke viral vector
837 core. The AAV9-EFS-NC-DIO-SpCas9-myc-NLS-Poly(A) (2.31x+e^{13}), AAV9-hPGK-DIO-
838 SpCas9-myc-NLS-Poly(A) (2.31x+e^{13}), AAV1-4xgRNAs$_{scramble}$-hSyn flex-GCaMP8s-wpre
839 (2.75x e^{12}) and AAV1-4xgRNAs $_{Oxtr/1Avp1ra}$ -hSyn flex- GCaMP8s-wpre 2.44x e^{12}) were packaged
840 at the HHMI Janelia Research Campus virus. The 4xgRNAs$_{scramble}$-ubc DsRed (TU/ML 1.5X e^{8})
841 and 4xgRNAs$_{Oxtr/Avp1ra}$ ubc DsRed (OXTR/AVP1Ra) lentiviruses (TU/ML 3.50 X e^{8}) were also
842 packaged at the HHMI Janelia Research Campus virus facility.

843

844 METHOD DETAILS

845 **Generation of multiplex CRISPR/*Streptococcus pyogenes* Cas9 vectors**

846 The multiplex gRNAs construct was based on the backbone of pLV GG hUbC-dsRED (addgene
847 #84034) after being modified to remove superfluous sequences (e.g., LoxP). Individual gRNAs
848 were cloned as described in *Kabadi et al., 2014*[73]. Cas9 pAAV-EFS-NC-SpCas9-NLS-Poly(A)
849 (Duke viral vector core) vectors were used for constitutive Cas9 expression. For Cre-dependent
850 CRISPR/Cas9 DIO/FLEX, sequences were cloned in pAAV-EFS-NC-Cas9-NLS-Poly(A) vectors,
851 respectively. The Golden Gate cassette to express four gRNAs was cloned into the pGP-AAV-
852 syn-FLEX-jGCaMP8s-WPRE (addgene 162377)[114] vector. Four different gRNAs are
853 constitutively being expressed under four different polymerase llI promoters, and a Cre-dependent

854 expression of the calcium indicator jGCaMP8s under the express human synapsing promoter.

855

856 **Generation of Neuro2A constitutively expressed CAS9 cells and screening of gRNAs**

857 Neuro2a cells (ATCC CCL-131™) were transfected with EFS-Cas9-Blast plasmid (addgene #
858 52962) and selected for four days with blasticidin antibiotic. Individual gRNAs were cloned in
859 ph7SK-gRNA (addgene # 53189) or phH1-gRNA (addgene # 53186) or pmU6-gRNA (addgene #
860 53187) or phU6-gRNA (addgene # 53188) plasmids, 0.5-1 ug transfected in Neuro2a-Cas9 cells
861 and after three days genomic DNA was isolated. We used T7 endonuclease assay for testing the
862 efficiency of each gRNAs to generate edits, similar to what has been described in
863 https://www.neb.com/protocols/2014/08/11/determining-genome-targeting-efficiency-using-t7-
864 endonuclease-i. In addition, Sanger traces were generated with target-specific PCR and analyzed
865 with the Tracking of INDELs by Decomposition (TIDE) web tool http://tide.nki.nl (data not
866 shown).

867

868 **Screening for aggressor male and resident intruder assay**

869 All experimental male mice (''residents'') were individually housed for two weeks and received
870 sexual experience (for at least one week). Previously it has been reported that ~20-25% of inbreeding
871 C57BL/6N male animals fail to display territorial aggression against conspecific male intruders
872 during the RI assay [115]. We pre-screened males for baseline aggression using resident-intruder testing
873 sessions to identify and exclude no aggressors from our analysis. Animals that attacked two
874 constitutively presented intruders were termed aggressors and added to the pool of animals for
875 CRISRP/Cas9-based gene editing surgeries. On the experimental day, the preselected male residents
876 were transported in their home cage to a novel behavioral testing room (under infrared light), where

877 they acclimated for 5-10 min. An unfamiliar group housed BALB/c mouse (‘‘intruder’’) was then
878 placed in the resident's home cage, and residents were allowed to interact with it for period of time.

879

880 **Acute brain slices preparation**

881 Briefly, male adult mice were anesthetized with isoflurane and transcardially perfused with cold
882 NMDG-ACSF (adjusted to pH 7.3–7.4) containing CaCl2 (0.5 mM), glucose (25 mM), HCl (92
883 mM), HEPES (20 mM), KCl (2.5 mM), kynurenic acid (1 mM), MgSO4 (10 mM), NaHCO3 (30
884 mM), NaH2PO4 (1.2 mM), NMDG (92 mM), sodium L-ascorbate (5 mM), sodium pyruvate (3
885 mM), thiourea (2 mM), bubbled with carbogen gas (95% O_2 and 5% CO_2). The brain was sectioned
886 at 250 µm using a vibratome (VT1000S, Leica Microsystems) on ice and was incubated in 34oc for
887 12 min, in NMDG – ACSF. Then transfer the sections to room temperature in aCSF/HEPES-GSH
888 solution (adjusted to pH 7.3–7.4,) containing CaCl2(2 mM), glucose (25 mM), kCl (2.5 mM),
889 HEPES (20 mM), NaCl (92 mM), MgSO4 (2 mM), NaHCO3 (30 mM), NaH2PO4 (1.2 mM),
890 sodium L-ascorbate (5 mM), sodium pyruvate (3 mM), thiourea (2 mM), and Glutathione Monoethyl
891 Ester (0.5-1mM)-before proceeding with Ca^{2+} imaging.

892

893 **Peptide perfusion and two-photon calcium imaging experiments**

894 Solutions of 100nM or 400nM of Oxt, Avp, and Oxt + Avp peptides were prepared in aCSF and
895 perfused with a rate of 1-2ml/min through a microfluidics chamber containing the brain slices.
896 Calcium imaging was performed using a custom-modified Ultima two-photon laser scanning

897 microscope (Bruker). The primary beam path was equipped with galvanometers driving a
898 Chameleon Ultra II Ti:Sapphire laser (Coherent) and used for GCaMP imaging (920 nm). GCaMP
899 emission was detected with photomultiplier-tube (Hamamatsu). Images were acquired with an
900 Olympus20X XLUMPLFLN Objective, 1.00 NA, 2.0 mm WD. All image acquisition was
901 performed using PrairieView Software (Version 5.3) with a framerate of ~1.2Hz.

902

903 **Behavior recording**

904 All behavioral experiments were performed in conventional mouse housing cages (home cage or
905 new cage) under red lighting, using the previously described behavior recording setup [116]. The
906 behavior video's top and front views were acquired at 30 Hz using the video recording software,
907 StreamPix7 (Norpix).

908 **Behavior annotations**

909 Behavior videos were processed using an automated behavior classification system to generate
910 frame-by-frame annotations of attack, mounting and sniffing behavior [117]. The output of the
911 classifier and behavior videos were loaded into a MATLAB based MATLAB-based behavior
912 annotation interface and then manually corrected by trained individuals to produce a final set of
913 annotations[117]. A 'baseline' period of 5-minutes was recorded at the start of every recording session
914 during which the animal was alone in its home cage. Six behaviors were annotated during the resident
915 intruder assays: sniff (face, body, genital-directed sniffing), towards male or female intruders, and
916 attack, mount with male or female intruders. For quantifying the interval (s) between behavioral
917 bouts in Figures 2, 3, S2 and S3 animals that didn't show any mount or attack behavior were

918 excluded. 15 min for male-male interaction was scored in Figure 2 and S2. In Figure 3 and S3 ~20
919 min of RI was scored for male -male interaction. 10 min of male-female interaction was scored
920 during the RI assays in Figure 2, 3, S2 and S3.

921 In addition to the classification of behaviors, automated pose estimation was performed on
922 behavior videos to obtain key points of interacting mice[117]. The velocity of the resident mouse was
923 calculated as the change in positions of centroids of the head and hips, computed across two
924 consecutive frames as previously performed[58,117]. The distribution of this feature was computed
925 for both experimental and control animals to obtain the data shown in Supplementary Figure
926 S2C(iii).

927 **Stereotaxic surgery**

928 Surgeries were performed on socially and sexually experienced adult male *Esr1*$^{Cre/+}$ mice and *Oxtr*
929 $^{cre/+}$ mice 8–12 weeks old. Virus injection and implantation were performed as described
930 previously [58,59]. Briefly, animals were anesthetized with isoflurane (5% for induction and 1.5% for
931 maintenance) and placed on a stereotaxic frame (David Kopf Instruments). The virus was injected
932 into the target area using a pulled-glass capillary (World Precision Instruments) and a pressure
933 injector (Micro4 controller, World Precision Instruments) at a 20 nl /min flow rate. The glass
934 capillary was left in place for 5 -10 minutes following injection before withdrawal. The injection
935 volumes were ~400-500nl for bilateral injection in mice used for behavioral analysis and
936 CRISRPometry. For micro endoscope recordings, we performed unilateral ~200nl injections. The
937 Stereotaxic injection coordinates were based on the Paxinos and Franklin atlas (VMHvl, anterior–
938 posterior: −4.68, medial–lateral: ±0.73, dorsal–ventral: −5.73). For single fiber optogenetic and
939 fiber photometry experiments (optogenetics: diameter 200 μm, N.A., 0.22; fiber photometry:

940 diameter 400 μm, N.A., 0.48; Doric lenses) were then placed above the virus injection sites (fiber
941 photometry: 150 μm above) and fixed on the skull with dental cement (Metabond, Parkell). For
942 micro-endoscope experiments, virus injection and lens implantation were performed on the same
943 day Lenses with a baseplate were slowly lowered into the brain and fixed to the skull with dental
944 cement. Mice were habituated with weight-matched dummy micro-endoscopes (Inscopix) for at
945 least one week before behavior testing. Mice were head-fixed on a running wheel 3-4 weeks after
946 lens implantation, and a miniaturized micro-endoscope (nVista, Inscopix) was attached to the
947 baseplate for imaging. Mice were singly housed after surgery and were allowed to recover for at
948 least 4 weeks before behavioral testing.
949

950 **Histology**

951 Once the behavioral experiments were finished, virus expression and implant placement were
952 histologically verified on all mice. Mice lacking correct virus expression or implant placement
953 were excluded from the analysis. Mice were transcardially perfused with 1x PBS at room
954 temperature, followed by 4% paraformaldehyde (PFA) (diluted from 16% EM grade PFA). Brains
955 were extracted and post-fixed in 4% PFA 16-24h at 4°C, followed by 24 hours in 30% sucrose/PBS
956 at 4 °C. Brains were embedded in OCT mounting medium, frozen on dry ice and stored at −80°C
957 for subsequent sectioning. Brains were sectioned into 60 μm slices on a cryostat (Leica
958 Biosystems). Sections were washed with 1× PBS and mounted on Superfrost slides, then incubated
959 for 15 minutes at room temperature in DAPI/PBS (0.5 μg/ml) for counterstaining, rewashed and
960 coverslipped. Sections were imaged with an epifluorescent microscope (Olympus VS120)
961 For some epitope staining 30 um sections were cut from either fresh-frozen tissue or post-fixed 2h
962 4%PFA on ice, immersed in 30% sucrose:1xPBS 4C 2h before embedding in OCT. For Cas9

963 immunostaining, a cocktail of antibodies against the epitope and the Cas9 protein was used.
964 Animals were stained after 9-12 weeks post-injection.

965

966 **Fiberphotometry recordings.**

967 The fiber photometry setup was similar to what was previously described [118]. We used 470 nm
968 LEDs (M470F3, Thorlabs, filtered with 470-10 nm bandpass filters FB470-10, Thorlabs) for
969 fluorophore excitation and 405 nm LEDs for isosbestic excitation (M405FP1, Thorlabs, filtered
970 with 410–10 nm bandpass filters FB410-10, Thorlabs). LEDs were modulated at 208 Hz (470 nm)
971 and 333 Hz (405 nm) and controlled by a real-time processor (RZ5P, Tucker David Technologies)
972 via an LED driver (DC4104, Thorlabs). The emission signal from the 470 nm excitation was
973 normalized to the emission signal from the isosbestic excitation (405 nm), to control for motion
974 artifacts, photobleaching, and levels of GCaMP8s expression. LEDs were coupled to a 425 nm
975 longpass dichroic mirror (Thorlabs, DMLP425R) via fiber optic patch cables (diameter 400 µm,
976 N.A., 0.48; Doric lenses). Emitted light was collected via the patch cable, coupled to a 490 nm
977 long pass dichroic mirror (DMLP490R, Thorlabs), filtered (FF01-542/27-25, Sem- rock),
978 collimated through a focusing lens (F671SMA-405, Thorlabs) and detected by the photodetectors
979 (Model 2151, Newport). Recordings were acquired using Synapse software (Tucker Davis
980 Technologies). On the test day, after at least 5 minutes of acclimation under the recording setup,
981 the male resident was first recorded for 1 minute to establish a baseline. Male or female intruders
982 were introduced into the home cage on separate days. Typically, each session lasted 15-20 min.
983

984 **Microendoscope recordings**

985 On the day of imaging, mice were habituated for at least 5-10 minutes after installing the micro
986 endoscope in their home cage before the start of the behavior tests. Imaging data were acquired at
987 30 Hz with 2× spatial down sampling; light-emitting diode power (0.1–0.5) and gain (1–7×) were
988 adjusted depending on the brightness of GCaMP expression as determined by the image histogram
989 according to the user manual. A transistor–transistor logic (TTL) pulse from the Sync port of the
990 data acquisition box (DAQ, Inscopix) was used for synchronous triggering of StreamPix7 (Norpix)
991 for video recording. Imaging sessions typically lasted 1 h (20–25 min interactions per sex).

992 **Micro-endoscopic data extraction**

993 Preprocessing and Calcium data extraction was performed similarly to what has been previously
994 described [57]. Briefly, data were 2x downsampled, motion corrected, and a spatial band-pass filter
995 was applied to remove the out-of-focus background. Next, filtered imaging data were temporally
996 downsampled to 10 Hz. Calcium traces were extracted and deconvolved using the CNMF-E [119]
997 with the following parameters: patch_dims = [42, 42], gSig = 3, gSiz = 13, ring_radius = 19,
998 min_corr ~0.57-0.62, min_pnr = ~5.5-6, deconvolution: foopsi with the ar1 model44. Every
999 extracted unit's spatial and temporal components were manually inspected (SNR, PNR, size,
1000 motion artifacts, decay kinetics, etc.). Traces of units were either z-scored or normalized in units
1001 of σ relative to the baseline fluorescence (during 7sec or more) of the neuron before the first trial
1002 of resident-intruder interactions, as previously described[57,58], Distinct hypothalamic control of
1003 same-and opposite-sex mounting behavior in mice. In Supplementary Figure 5 C, the z-scored
1004 value during a behavioral bout for each unit was normalized by subtracting the mean of a 2-3 sec
1005 baseline before the onset of the bout. The average normalized activity was quantified for a period
1006 of 15 sec. A total of 585 units (n=5 mice) from control and 546 units (n=7 mice) from experimental
1007 mice were recorded.

1008 **Quantification and statistical analysis**

1009 **Transcriptomic analysis of *Esr1*, *Oxtr*, *Avpr1a* mRNAs**

1010 The violin plots, t-SNE and the quantification of *Esr1*, *Oxtr*, *Avpr1a* mRNAs in the different single
1011 cell VMH clusters (Figure 1B, S1B and S1D) or in single Esr1+ cells (Figure 1D) was performed
1012 with R package Seurat as described previously[69].

1013

1014 **Fiberphotometry analysis**

1015 All data analyses were performed in Matlab 2020a and Python 3.8.3 as previously described[58].
1016 Briefly, behavioral video files and fiber photometry data were obtained in a time-locked manner.
1017 Photometry recordings yielded both a 405-nm (isosbestic, Ca^{2+} independent) signal and a 470-nm
1018 (Ca^{2+} dependent)) signal. To align the 405-nm signal to the 470-nm signal, a least squares linear
1019 fit is first performed. The motion corrected 470-nm signal is obtained as follows:
1020 $[\, F_{470}(\mathrm{t}) - F_{405}(\mathrm{t}) \,] \,/\, F_{405}(\mathrm{t})$. To normalize activity, the baseline value F_0 and standard deviation
1021 SD_0. were calculated using a 2 second window as follows $[\, F_n(\mathrm{t}) - F_0(\mathrm{t}) \,] \,/ SD_0$. Overlapping
1022 behavioral bouts within this time window were excluded from the analysis. The peak and area
1023 under the normalized activity curve (AUC) were calculated within the 10-second window. We
1024 confirmed that the latency to achieve the peri-stimulus time histogram (PETH) peak level is shorter
1025 than the indicated time window.

1026

1027 **Miniscope neural data analysis**

1028 **Choice probability**

1029 Choice probability (CP) analysis was used as before[58] to measure a cell's tuning, defined here as
1030 how well two conditions could be predictively discriminated from a single cell's activity [120]. The
1031 CP of a given cell for a pair of behavioral conditions was computed by constructing a histogram
1032 of that cell's $\Delta F(t)/F_0$ values under each of the two conditions. These two histograms were plotted
1033 against each other to generate a ROC (receiver-operating characteristic) curve. The integral of the
1034 area under this ROC curve generated the CP value for each cell with respect to each of the two
1035 behavioral conditions. This CP value is bounded from 0 to 1, where a CP of 0.5 indicates that the
1036 neuron's activity cannot distinguish between the two conditions. As in previous studies, the
1037 statistical significance of choice probabilities was determined relative to chance. We shuffled
1038 behavioral bout timings for each of the two compared conditions and computed the choice
1039 probability for this shuffled data. Shuffling was repeated 100 times for each of the two behaviors,
1040 from which we calculated the mean and s.d. (σ) of the 'shuffled' choice probabilities.

1041 As significant, we considered any observed choice probabilities $>2\sigma$ above the shuffled mean and
1042 imposed an additional choice probability threshold > 0.7 as previously described[58]. The colored
1043 bars indicate the neurons that show a strong and statistically significant choice probability, and
1044 grey bars indicate cells for which the choice probability was either activated $< 2\ \sigma$ above (not
1045 responsive) the shuffled mean or was considered which choice probability not significantly higher
1046 than chance or choice probability ≤ 0.7 for that neuron.

1047 **Dimensionality reduction for visualizing intruder sex**

1048 Low-dimensional representations for visualizing changing ensemble dynamics over time were
1049 constructed using partial least squares (PLS) regression (MATLAB). For PLS, all traces were

1050 concatenated and regressed against a $1 \times T$ vector with entries valued at −1 (if a male intruder
1051 was present), 1 (if there was a female intruder), or 0 (otherwise).

1052 **Decoding intruder sex from neural data**

1053 We constructed a frame-wise linear SVM decoders (as described previously[58,59]) to distinguish
1054 intruder sex. Training data was constructed from the set of $N \times 1$ (N = neurons) population
1055 activity vectors from all frames occurring during social interaction in each mouse. Equal
1056 numbers of frames of male and female interaction were used during decoder training to ensure
1057 chance decoder performance of 50%. Shuffled decoder data were generated by the training the
1058 decoder on the same neural data but with behavior labels randomly assigned to each behavior
1059 bout (n=5 control and n=7 *expreimental mice*). This training data, along with intruder sex labels,
1060 was then used to train a linear SVM decoder. Accuracy was evaluated using a stratified fivefold
1061 cross-validator. Decoding was repeated 100 times, with decoder performance reported as the
1062 mean accuracy per imaged animal. For significance testing, the mean accuracy of the decoder
1063 trained on shuffled data (repeated 500 times per imaged animal) was computed to compare
1064 against the decoder accuracy trained on actual data.

1065 **Decoding behavior from neural activity**

1066 We constructed frame-wise linear SVM decoders (as described previously[57,58]) to discriminate
1067 male directed sniffing and attack from imaged control and experimental VMHvl^{Esr1} units. Briefly
1068 manual annotations of sniffing behavior and attack behavior for each intruder male mouse were
1069 used to provide training labels of behavior type in control and experimental mice. Bar graphs of
1070 decoder accuracy (Figure S5E) were generated to discriminate sniffing and attack from imaged
1071 activity on individual frames of a behavior (sampled at 15 Hz). Equal numbers of sniff and attack

1072 frames (frame-wise decoder) were used during decoder training, to ensure chance decoder
1073 performance of 50%. 'Shuffled' decoder data were generated by training the decoder on the
1074 same neural data, but with sniff and attack behavior annotations randomly assigned to each
1075 behavior bout.

1076 Decoding was repeated 20 times for each intruder and each imaged mouse, and decoder
1077 performance was reported as the average accuracy across imaged mice for control and
1078 experimental mice. For significance testing, the mean accuracy of the decoder trained on
1079 shuffled data was computed across mice, in each condition, and shuffling was repeated 1,000
1080 times. Significance was determined across imaged mice using the Mann–Whitney U test between
1081 the mean accuracy of the decoders trained on real versus shuffled data.

1082 **Statistical analysis**

1083 Data were processed and analyzed using Python, MATLAB and GraphPad (GraphPad
1084 PRISM v.9). Data were analyzed using two-tailed, nested non-parametric tests. Wilcoxon signed-
1085 rank test (paired, non-parametric Mann–Whitney *U*-test) was used for binary paired samples.
1086 Kolmogorov–Smirnov test was used for non-paired samples plotted as ECDF graphs.
1087 N.s. $P > 0.05$, *$P < 0.05$, **$P < 0.01$, ***$P < 0.001$, ****$P < 0.0001$.

1088 **Dynamical system models of neural data**

1089 As previously described in published work[20], we modeled neural activity using recurrent switching
1090 linear dynamical systems (rSLDS). Briefly, rSLDS is a generative model that breaks down non-
1091 linear time series data into sequences of linear dynamical modes. The model relates three sets of
1092 variables: a set of discrete states (z), a set of continuous latent factors (x) that captures the low-

dimensional nature of neural activity, and the activity of recorded neurons (y). The model also allows for external inputs (u), which consist of extracted pose features, including the distance between animals and the facing angle between the resident and intruder mouse. For how the model is formulated, see Nair, et al., 2023[20]. Model accuracy is evaluated using a forward simulation metric as described in Nair et al., 2023[20]. Briefly: given the observed neural activity at time t, we predict the trajectory of the population activity vector over an ensuing short time interval Δt using the model, then compute the mean squared error (MSE) between that trajectory and the observed data at time $t + \Delta t$. This MSE is calculated across all dimensions of the latent space and repeated for all times t. This error metric is normalized to a 0-1 range in each animal across the whole recording and is computed across cross-validation folds to obtain a bounded measure of model performance.

Code used to fit rSLDS on neural data is available in the SSM package: (https://github.com/lindermanlab/ssm)

Code to generate flow fields and energy landscapes from fit dynamical systems is available at (https://github.com/DJALab/VMHvl_MPOA_dynamics)

Visualization of attractor dynamics as 3D landscape

Conversion of the flow-fields obtained from rSLDS into a 3D landscape for visualization by calculating the dynamic velocity at each point in neural state space and using it as the height of a 3D landscape. Dynamic velocity was calculated as previously reported in *Nair et al., 2022.*

Estimation of time constants & calculation of line attractor score.

We estimated the time constant of each mode of linear dynamical systems using eigenvalues λ_a of the dynamics matrix of that system as: $\tau_a = \left|\frac{1}{\log(|\lambda_a|)}\right|$ as derived by Maheswaranathan et al., 2019 [121]. We used a line attractor score computed as $\log_2 \frac{t_n}{t_{n-1}}$ where t_n is the largest time constant of the dynamics matrix of a dynamical system andt_{n-1} is the second largest time constant. In the case of point attractors, the line attractor score is zero due to the similar magnitudes of the first two largest time constants, and it is greater than one for systems that possess a line attractor.

REFERENCES

1. Sternson, S.M. (2013). Hypothalamic survival circuits: blueprints for purposive behaviors. Neuron *77*, 810-824. 10.1016/j.neuron.2013.02.018.
2. Anderson, D.J., and Adolphs, R. (2014). A framework for studying emotions across species. Cell *157*, 187-200. 10.1016/j.cell.2014.03.003.
3. Zych, A.D., and Gogolla, N. (2021). Expressions of emotions across species. Curr Opin Neurobiol *68*, 57-66. 10.1016/j.conb.2021.01.003.
4. Damasio, A., and Carvalho, G.B. (2013). The nature of feelings: evolutionary and neurobiological origins. Nature reviews Neuroscience *14*, 143-152. 10.1038/nrn3403.
5. Dolan, R.J. (2002). Emotion, cognition, and behavior. Science *298*, 1191-1194.
6. Flavell, S.W., Gogolla, N., Lovett-Barron, M., and Zelikowsky, M. (2022). The emergence and influence of internal states. Neuron *110*, 2545-2570. 10.1016/j.neuron.2022.04.030.
7. Malezieux, M., Klein, A.S., and Gogolla, N. (2023). Neural Circuits for Emotion. Annu Rev Neurosci *46*, 211-231. 10.1146/annurev-neuro-111020-103314.
8. Anderson, D.J. (2016). Circuit modules linking internal states and social behaviour in flies and mice. Nat Rev Neurosci *17*, 692-704. 10.1038/nrn.2016.125.
9. Deisseroth, K. (2014). Circuit dynamics of adaptive and maladaptive behaviour. Nature *505*, 309-317. 10.1038/nature12982.
10. Xu, S., Yang, H., Menon, V., Lemire, A.L., Wang, L., Henry, F.E., Turaga, S.C., and Sternson, S.M. (2020). Behavioral state coding by molecularly defined paraventricular hypothalamic cell type ensembles. Science *370*. 10.1126/science.abb2494.
11. Kennedy, A., Kunwar, P.S., Li, L., Stagkourakis, S., Wagenaar, D.A., and Anderson, D.J. (2020). Stimulus-specific hypothalamic encoding of a persistent defensive state. Nature *586*, 730-734.
12. Augustine, V., Lee, S., and Oka, Y. (2020). Neural Control and Modulation of Thirst, Sodium Appetite, and Hunger. Cell *180*, 25-32. 10.1016/j.cell.2019.11.040.
13. Jazayeri, M., and Afraz, A. (2017). Navigating the Neural Space in Search of the Neural Code. Neuron *93*, 1003-1014. 10.1016/j.neuron.2017.02.019.
14. Ebitz, R.B., and Hayden, B.Y. (2021). The population doctrine in cognitive neuroscience. Neuron *109*, 3055-3068. 10.1016/j.neuron.2021.07.011.
15. Shenoy, K.V., Sahani, M., and Churchland, M.M. (2013). Cortical control of arm movements: a dynamical systems perspective. Annual review of neuroscience *36*, 337-359.
16. Mante, V., Sussillo, D., Shenoy, K.V., and Newsome, W.T. (2013). Context-dependent computation by recurrent dynamics in prefrontal cortex. nature *503*, 78-84.
17. Khona, M., and Fiete, I.R. (2022). Attractor and integrator networks in the brain. Nat Rev Neurosci. 10.1038/s41583-022-00642-0.
18. Inagaki, H.K., Chen, S., Daie, K., Finkelstein, A., Fontolan, L., Romani, S., and Svoboda, K. (2022). Neural Algorithms and Circuits for Motor Planning. Annu Rev Neurosci *45*, 249-271. 10.1146/annurev-neuro-092021-121730.
19. Liu, M., Nair, A., Linderman, S.W., and Anderson, D.J. (2023). Periodic hypothalamic attractor-like dynamics during the estrus cycle. bioRxiv. 10.1101/2023.05.22.541741.

20. Nair, A., Karigo, T., Yang, B., Ganguli, S., Schnitzer, M.J., Linderman, S.W., Anderson, D.J., and Kennedy, A. (2023). An approximate line attractor in the hypothalamus encodes an aggressive state. Cell *186*, 178-193 e115. 10.1016/j.cell.2022.11.027.
21. Sylwestrak, E.L., Jo, Y., Vesuna, S., Wang, X., Holcomb, B., Tien, R.H., Kim, D.K., Fenno, L., Ramakrishnan, C., Allen, W.E., et al. (2022). Cell-type-specific population dynamics of diverse reward computations. Cell *185*, 3568-3587 e3527. 10.1016/j.cell.2022.08.019.
22. Langdon, C., Genkin, M., and Engel, T.A. (2023). A unifying perspective on neural manifolds and circuits for cognition. Nat Rev Neurosci *24*, 363-377. 10.1038/s41583-023-00693-x.
23. Hulse, B.K., and Jayaraman, V. (2020). Mechanisms underlying the neural computation of head direction. Annual review of neuroscience *43*, 31-54.
24. Kim, S.S., Rouault, H., Druckmann, S., and Jayaraman, V. (2017). Ring attractor dynamics in the Drosophila central brain. Science *356*, 849-853. 10.1126/science.aal4835.
25. Inagaki, H.K., Chen, S., Ridder, M.C., Sah, P., Li, N., Yang, Z., Hasanbegovic, H., Gao, Z., Gerfen, C.R., and Svoboda, K. (2022). A midbrain-thalamus-cortex circuit reorganizes cortical dynamics to initiate movement. Cell *185*, 1065-1081 e1023. 10.1016/j.cell.2022.02.006.
26. Goldman, M., Compte, A., and Wang, X.-J. (2007). Neural integrators: recurrent mechanisms and models. New Encyclopedia of Neuroscience, 1-26.
27. Major, G., and Tank, D. (2004). Persistent neural activity: prevalence and mechanisms. Curr Opin Neurobiol *14*, 675-684. 10.1016/j.conb.2004.10.017.
28. Turner-Evans, D.B., Jensen, K.T., Ali, S., Paterson, T., Sheridan, A., Ray, R.P., Wolff, T., Lauritzen, J.S., Rubin, G.M., Bock, D.D., and Jayaraman, V. (2020). The Neuroanatomical Ultrastructure and Function of a Biological Ring Attractor. Neuron *108*, 145-163 e110. 10.1016/j.neuron.2020.08.006.
29. Lockard, M.A., Ebert, M.S., and Bargmann, C.I. (2017). Oxytocin mediated behavior in invertebrates: An evolutionary perspective. Dev Neurobiol *77*, 128-142. 10.1002/dneu.22466.
30. Zelikowsky, M., Ding, K., and Anderson, D.J. (2018). Neuropeptidergic Control of an Internal Brain State Produced by Prolonged Social Isolation Stress. Cold Spring Harb Symp Quant Biol *83*, 97-103. 10.1101/sqb.2018.83.038109.
31. Wang, P., Wang, S.C., Liu, X., Jia, S., Wang, X., Li, T., Yu, J., Parpura, V., and Wang, Y.F. (2022). Neural Functions of Hypothalamic Oxytocin and its Regulation. ASN Neuro *14*, 17590914221100706. 10.1177/17590914221100706.
32. Koppan, M., Nagy, Z., Bosnyak, I., and Reglodi, D. (2022). Female reproductive functions of the neuropeptide PACAP. Front Endocrinol (Lausanne) *13*, 982551. 10.3389/fendo.2022.982551.
33. Asahina, K., Watanabe, K., Duistermars, B.J., Hoopfer, E., González, C.R., Eyjólfsdóttir, E.A., Perona, P., and Anderson, D.J. (2014). Tachykinin-Expressing Neurons Control Male-Specific Aggressive Arousal in Drosophila. Cell *156*, 221-235. 10.1016/j.cell.2013.11.045.
34. Siegel, A., Roeling, T.A., Gregg, T.R., and Kruk, M.R. (1999). Neuropharmacology of brain-stimulation-evoked aggression. Neuroscience & Biobehavioral Reviews *23*, 359-389.
35. Zelikowsky, M., Hui, M., Karigo, T., Choe, A., Yang, B., Blanco, M.R., Beadle, K., Gradinaru, V., Deverman, B.E., and Anderson, D.J. (2018). The Neuropeptide Tac2 Controls a

1219 Distributed Brain State Induced by Chronic Social Isolation Stress. Cell *173*, 1265-1279
1220 e1219. 10.1016/j.cell.2018.03.037.
1221 36. Lim, M.M., and Young, L.J. (2006). Neuropeptidergic regulation of affiliative behavior and
1222 social bonding in animals. Horm Behav *50*, 506-517. 10.1016/j.yhbeh.2006.06.028.
1223 37. Sohn, J.W., Elmquist, J.K., and Williams, K.W. (2013). Neuronal circuits that regulate
1224 feeding behavior and metabolism. Trends Neurosci *36*, 504-512.
1225 10.1016/j.tins.2013.05.003.
1226 38. Bowers, M.E., Choi, D.C., and Ressler, K.J. (2012). Neuropeptide regulation of fear and
1227 anxiety: Implications of cholecystokinin, endogenous opioids, and neuropeptide Y. Physiol
1228 Behav *107*, 699-710. 10.1016/j.physbeh.2012.03.004.
1229 39. Marder, E. (2012). Neuromodulation of neuronal circuits: back to the future. Neuron *76*,
1230 1-11. 10.1016/j.neuron.2012.09.010.
1231 40. Nusbaum, M.P., Blitz, D.M., and Marder, E. (2017). Functional consequences of
1232 neuropeptide and small-molecule co-transmission. Nat Rev Neurosci *18*, 389-403.
1233 10.1038/nrn.2017.56.
1234 41. Bargmann, C.I., and Marder, E. (2013). From the connectome to brain function. Nature
1235 Methods *10*, 483-490. 10.1038/nmeth.2451.
1236 42. Flavell, S.W., Pokala, N., Macosko, E.Z., Albrecht, D.R., Larsch, J., and Bargmann, C.I.
1237 (2013). Serotonin and the neuropeptide PDF initiate and extend opposing behavioral
1238 states in C. elegans. Cell *154*, 1023-1035. 10.1016/j.cell.2013.08.001.
1239 43. Ji, N., Madan, G.K., Fabre, G.I., Dayan, A., Baker, C.M., Kramer, T.S., Nwabudike, I., and
1240 Flavell, S.W. (2021). A neural circuit for flexible control of persistent behavioral states.
1241 Elife *10*. 10.7554/eLife.62889.
1242 44. Kato, S., Kaplan, H.S., Schrödel, T., Skora, S., Lindsay, T.H., Yemini, E., Lockery, S., and
1243 Zimmer, M. (2015). Global Brain Dynamics Embed the Motor Command Sequence of
1244 Caenorhabditis elegans. Cell, 656-669. 10.1016/j.cell.2015.09.034.
1245 45. Hallinen, K.M., Dempsey, R., Scholz, M., Yu, X., Linder, A., Randi, F., Sharma, A.K., Shaevitz,
1246 J.W., and Leifer, A.M. (2021). Decoding locomotion from population neural activity in
1247 moving C. elegans. Elife *10*. 10.7554/eLife.66135.
1248 46. Andalman, A.S., Burns, V.M., Lovett-Barron, M., Broxton, M., Poole, B., Yang, S.J.,
1249 Grosenick, L., Lerner, T.N., Chen, R., Benster, T., et al. (2019). Neuronal Dynamics
1250 Regulating Brain and Behavioral State Transitions. Cell *177*, 970-985 e920.
1251 10.1016/j.cell.2019.02.037.
1252 47. Allen, W.E., Chen, M.Z., Pichamoorthy, N., Tien, R.H., Pachitariu, M., Luo, L., and
1253 Deisseroth, K. (2019). Thirst regulates motivated behavior through modulation of
1254 brainwide neural population dynamics. Science *364*, 253. 10.1126/science.aav3932.
1255 48. Heidenreich, M., and Zhang, F. (2016). Applications of CRISPR-Cas systems in
1256 neuroscience. Nat Rev Neurosci *17*, 36-44. 10.1038/nrn.2015.2.
1257 49. Ziv, Y., Burns, L.D., Cocker, E.D., Hamel, E.O., Ghosh, K.K., Kitch, L.J., El Gamal, A., and
1258 Schnitzer, M.J. (2013). Long-term dynamics of CA1 hippocampal place codes. Nat
1259 Neurosci *16*, 264-266. 10.1038/nn.3329.
1260 50. Zha, X., and Xu, X.H. (2021). Neural circuit mechanisms that govern inter-male attack in
1261 mice. Cell Mol Life Sci *78*, 7289-7307. 10.1007/s00018-021-03956-x.

1262 51. Froemke, R.C., and Young, L.J. (2021). Oxytocin, Neural Plasticity, and Social Behavior.
1263 Annu Rev Neurosci *44*, 359-381. 10.1146/annurev-neuro-102320-102847.
1264 52. de Jong, T.R., and Neumann, I.D. (2018). Oxytocin and Aggression. Curr Top Behav
1265 Neurosci *35*, 175-192. 10.1007/7854_2017_13.
1266 53. Lischinsky, J.E., and Lin, D. (2020). Neural mechanisms of aggression across species. Nat
1267 Neurosci *23*, 1317-1328. 10.1038/s41593-020-00715-2.
1268 54. Lin, D., Boyle, M.P., Dollar, P., Lee, H., Lein, E.S., Perona, P., and Anderson, D.J. (2011).
1269 Functional identification of an aggression locus in the mouse hypothalamus. Nature *470*,
1270 221-226. 10.1038/nature09736.
1271 55. Lee, H., Kim, D.W., Remedios, R., Anthony, T.E., Chang, A., Madisen, L., Zeng, H., and
1272 Anderson, D.J. (2014). Scalable control of mounting and attack by Esr1+ neurons in the
1273 ventromedial hypothalamus. Nature *509*, 627-632. 10.1038/nature13169.
1274 56. Yang, C.F., Chiang, M.C., Gray, D.C., Prabhakaran, M., Alvarado, M., Juntti, S.A., Unger,
1275 E.K., Wells, J.A., and Shah, N.M. (2013). Sexually dimorphic neurons in the ventromedial
1276 hypothalamus govern mating in both sexes and aggression in males. Cell *153*, 896-909.
1277 10.1016/j.cell.2013.04.017.
1278 57. Yang, B., Karigo, T., and Anderson, D.J. (2022). Transformations of neural representations
1279 in a social behaviour network. Nature *608*, 741-749. 10.1038/s41586-022-05057-6.
1280 58. Karigo, T., Kennedy, A., Yang, B., Liu, M., Tai, D., Wahle, I.A., and Anderson, D.J. (2021).
1281 Distinct hypothalamic control of same-and opposite-sex mounting behaviour in mice.
1282 Nature *589*, 258-263.
1283 59. Remedios, R., Kennedy, A., Zelikowsky, M., Grewe, B.F., Schnitzer, M.J., and Anderson,
1284 D.J. (2017). Social behaviour shapes hypothalamic neural ensemble representations of
1285 conspecific sex. Nature *550*, 388-392.
1286 60. Bale, T.L., Dorsa, D.M., and Johnston, C.A. (1995). Oxytocin receptor mRNA expression in
1287 the ventromedial hypothalamus during the estrous cycle. J Neurosci *15*, 5058-5064.
1288 10.1523/JNEUROSCI.15-07-05058.1995.
1289 61. Dumais, K.M., and Veenema, A.H. (2016). Vasopressin and oxytocin receptor systems in
1290 the brain: Sex differences and sex-specific regulation of social behavior. Front
1291 Neuroendocrinol *40*, 1-23. 10.1016/j.yfrne.2015.04.003.
1292 62. Delville, Y., Mansour, K.M., and Ferris, C.F. (1996). Testosterone facilitates aggression by
1293 modulating vasopressin receptors in the hypothalamus. Physiol Behav *60*, 25-29.
1294 10.1016/0031-9384(95)02246-5.
1295 63. Glaser, J., Whiteway, M., Cunningham, J.P., Paninski, L., and Linderman, S. (2020).
1296 Recurrent switching dynamical systems models for multiple interacting neural
1297 populations. Advances in neural information processing systems *33*, 14867-14878.
1298 64. Song, Z., and Albers, H.E. (2018). Cross-talk among oxytocin and arginine-vasopressin
1299 receptors: Relevance for basic and clinical studies of the brain and periphery. Front
1300 Neuroendocrinol *51*, 14-24. 10.1016/j.yfrne.2017.10.004.
1301 65. Szot, P., Bale, T.L., and Dorsa, D.M. (1994). Distribution of messenger RNA for the
1302 vasopressin V1a receptor in the CNS of male and female rats. Brain Res Mol Brain Res *24*,
1303 1-10. 10.1016/0169-328x(94)90111-2.
1304 66. Barberis, C., and Tribollet, E. (1996). Vasopressin and oxytocin receptors in the central
1305 nervous system. Crit Rev Neurobiol *10*, 119-154. 10.1615/critrevneurobiol.v10.i1.60.

1306 67. Newmaster, K.T., Nolan, Z.T., Chon, U., Vanselow, D.J., Weit, A.R., Tabbaa, M., Hidema,
1307 S., Nishimori, K., Hammock, E.A.D., and Kim, Y. (2020). Quantitative cellular-resolution
1308 map of the oxytocin receptor in postnatally developing mouse brains. Nat Commun *11*,
1309 1885. 10.1038/s41467-020-15659-1.
1310 68. Sharma, K., LeBlanc, R., Haque, M., Nishimori, K., Reid, M.M., and Teruyama, R. (2019).
1311 Sexually dimorphic oxytocin receptor-expressing neurons in the preoptic area of the
1312 mouse brain. PLoS One *14*, e0219784. 10.1371/journal.pone.0219784.
1313 69. Kim, D.-W., Yao, Z., Graybuck, L.T., Kim, T.K., Nguyen, T.N., Smith, K.A., Fong, O., Yi, L.,
1314 Koulena, N., Pierson, N., et al. (2019). Multimodal analysis of cell types in a hypothalamic
1315 node controlling social behavior. Cell *in press*.
1316 70. Dana, H., Sun, Y., Mohar, B., Hulse, B.K., Kerlin, A.M., Hasseman, J.P., Tsegaye, G., Tsang,
1317 A., Wong, A., Patel, R., et al. (2019). High-performance calcium sensors for imaging activity
1318 in neuronal populations and microcompartments. Nat Methods *16*, 649-657.
1319 10.1038/s41592-019-0435-6.
1320 71. Ragnauth, A.K., Goodwillie, A., Brewer, C., Muglia, L.J., Pfaff, D.W., and Kow, L.M. (2004).
1321 Vasopressin stimulates ventromedial hypothalamic neurons via oxytocin receptors in
1322 oxytocin gene knockout male and female mice. Neuroendocrinology *80*, 92-99.
1323 10.1159/000081844.
1324 72. Inenaga, K., Karman, H., Yamashita, H., Tribollet, E., Raggenbass, M., and Dreifuss, J.J.
1325 (1991). Oxytocin excites neurons located in the ventromedial nucleus of the Guinea-pig
1326 hypothalamus. J Neuroendocrinol *3*, 569-573. 10.1111/j.1365-2826.1991.tb00318.x.
1327 73. Kabadi, A.M., Ousterout, D.G., Hilton, I.B., and Gersbach, C.A. (2014). Multiplex
1328 CRISPR/Cas9-based genome engineering from a single lentiviral vector. Nucleic Acids Res
1329 *42*, e147. 10.1093/nar/gku749.
1330 74. Sarin, S., Zuniga-Sanchez, E., Kurmangaliyev, Y.Z., Cousins, H., Patel, M., Hernandez, J.,
1331 Zhang, K.X., Samuel, M.A., Morey, M., Sanes, J.R., and Zipursky, S.L. (2018). Role for Wnt
1332 Signaling in Retinal Neuropil Development: Analysis via RNA-Seq and In Vivo Somatic
1333 CRISPR Mutagenesis. Neuron *98*, 109-126 e108. 10.1016/j.neuron.2018.03.004.
1334 75. Sentmanat, M.F., Peters, S.T., Florian, C.P., Connelly, J.P., and Pruett-Miller, S.M. (2018).
1335 A Survey of Validation Strategies for CRISPR-Cas9 Editing. Sci Rep *8*, 888. 10.1038/s41598-
1336 018-19441-8.
1337 76. Ferris, C.F. (2005). Vasopressin/oxytocin and aggression. Molecular mechanisms
1338 influencing aggressive behaviours, 190-200.
1339 77. DeVries, A.C., Young, W.S., 3rd, and Nelson, R.J. (1997). Reduced aggressive behaviour in
1340 mice with targeted disruption of the oxytocin gene. J Neuroendocrinol *9*, 363-368.
1341 10.1046/j.1365-2826.1997.t01-1-00589.x.
1342 78. Wersinger, S.R., Caldwell, H.K., Martinez, L., Gold, P., Hu, S.B., and Young, W.S., 3rd
1343 (2007). Vasopressin 1a receptor knockout mice have a subtle olfactory deficit but normal
1344 aggression. Genes Brain Behav *6*, 540-551. 10.1111/j.1601-183X.2006.00281.x.
1345 79. Egashira, N., Tanoue, A., Matsuda, T., Koushi, E., Harada, S., Takano, Y., Tsujimoto, G.,
1346 Mishima, K., Iwasaki, K., and Fujiwara, M. (2007). Impaired social interaction and reduced
1347 anxiety-related behavior in vasopressin V1a receptor knockout mice. Behav Brain Res *178*,
1348 123-127. 10.1016/j.bbr.2006.12.009.

1349 80. Tuladhar, R., Yeu, Y., Tyler Piazza, J., Tan, Z., Rene Clemenceau, J., Wu, X., Barrett, Q.,
1350 Herbert, J., Mathews, D.H., Kim, J., et al. (2019). CRISPR-Cas9-based mutagenesis
1351 frequently provokes on-target mRNA misregulation. Nat Commun *10*, 4056.
1352 10.1038/s41467-019-12028-5.
1353 81. Hashikawa, K., Hashikawa, Y., Tremblay, R., Zhang, J., Feng, J.E., Sabol, A., Piper, W.T., Lee,
1354 H., Rudy, B., and Lin, D. (2017). Esr1(+) cells in the ventromedial hypothalamus control
1355 female aggression. Nat Neurosci *20*, 1580-1590. 10.1038/nn.4644.
1356 82. Egorov, A.V., Hamam, B.N., Fransen, E., Hasselmo, M.E., and Alonso, A.A. (2002). Graded
1357 persistent activity in entorhinal cortex neurons. Nature *420*, 173-178.
1358 10.1038/nature01171.
1359 83. Heys, J.G., Schultheiss, N.W., Shay, C.F., Tsuno, Y., and Hasselmo, M.E. (2012). Effects of
1360 acetylcholine on neuronal properties in entorhinal cortex. Front Behav Neurosci *6*, 32.
1361 10.3389/fnbeh.2012.00032.
1362 84. Linderman, S.J.M.M.A.A.R.B.D., and Paninski, L. (2017). Bayesian learning and inference
1363 in recurrent switching linear dynamical systems. Artificial Intelligence and Statistics
1364 (PMLR).
1365 85. Cavanagh, S.E., Towers, J.P., Wallis, J.D., Hunt, L.T., and Kennerley, S.W. (2018).
1366 Reconciling persistent and dynamic hypotheses of working memory coding in prefrontal
1367 cortex. Nat Commun *9*, 3498. 10.1038/s41467-018-05873-3.
1368 86. Murray, J.D., Bernacchia, A., Freedman, D.J., Romo, R., Wallis, J.D., Cai, X., Padoa-
1369 Schioppa, C., Pasternak, T., Seo, H., Lee, D., and Wang, X.J. (2014). A hierarchy of intrinsic
1370 timescales across primate cortex. Nat Neurosci *17*, 1661-1663. 10.1038/nn.3862.
1371 87. Doudna, J.A., and Charpentier, E. (2014). Genome editing. The new frontier of genome
1372 engineering with CRISPR-Cas9. Science *346*, 1258096. 10.1126/science.1258096.
1373 88. Melzer, S., Newmark, E.R., Mizuno, G.O., Hyun, M., Philson, A.C., Quiroli, E., Righetti, B.,
1374 Gregory, M.R., Huang, K.W., Levasseur, J., et al. (2021). Bombesin-like peptide recruits
1375 disinhibitory cortical circuits and enhances fear memories. Cell *184*, 5622-5634 e5625.
1376 10.1016/j.cell.2021.09.013.
1377 89. Bäck, S., Necarsulmer, J., Whitaker, L.R., Coke, L.M., Koivula, P., Heathward, E.J., Fortuno,
1378 L.V., Zhang, Y., Yeh, C.G., Baldwin, H.A., et al. (2019). Neuron-Specific Genome
1379 Modification in the Adult Rat Brain Using CRISPR-Cas9 Transgenic Rats. Neuron *102*, 105-
1380 119.e108. 10.1016/j.neuron.2019.01.035.
1381 90. Ma, C., Zhong, P., Liu, D., Barger, Z.K., Zhou, L., Chang, W.C., Kim, B., and Dan, Y. (2019).
1382 Sleep Regulation by Neurotensinergic Neurons in a Thalamo-Amygdala Circuit. Neuron
1383 *103*, 323-334 e327. 10.1016/j.neuron.2019.05.015.
1384 91. Newman, E.L., Gupta, K., Climer, J.R., Monaghan, C.K., and Hasselmo, M.E. (2012).
1385 Cholinergic modulation of cognitive processing: insights drawn from computational
1386 models. Front Behav Neurosci *6*, 24. 10.3389/fnbeh.2012.00024.
1387 92. Seung, H.S. (1996). How the brain keeps the eyes still. Proceedings of the National
1388 Academy of Sciences *93*, 13339-13344.
1389 93. Shao, Y.Q., Fan, L., Wu, W.Y., Zhu, Y.J., and Xu, H.T. (2022). A developmental switch
1390 between electrical and neuropeptide communication in the ventromedial hypothalamus.
1391 Curr Biol *32*, 3137-3145 e3133. 10.1016/j.cub.2022.05.029.

1392 94. Kunwar, P.S., Zelikowsky, M., Remedios, R., Cai, H., Yilmaz, M., Meister, M., and Anderson,
1393 D.J. (2015). Ventromedial hypothalamic neurons control a defensive emotion state. Elife
1394 *4*. 10.7554/eLife.06633.
1395 95. Wang, L., Chen, I.Z., and Lin, D. (2015). Collateral pathways from the ventromedial
1396 hypothalamus mediate defensive behaviors. Neuron *85*, 1344-1358.
1397 10.1016/j.neuron.2014.12.025.
1398 96. Silva, B.A., Mattucci, C., Krzywkowski, P., Murana, E., Illarionova, A., Grinevich, V.,
1399 Canteras, N.S., Ragozzino, D., and Gross, C.T. (2013). Independent hypothalamic circuits
1400 for social and predator fear. Nat Neurosci *16*, 1731-1733. 10.1038/nn.3573.
1401 97. Simerly, R.B. (1990). Hormonal control of neuropeptide gene expression in sexually
1402 dimorphic olfactory pathways. Trends Neurosci *13*, 104-110. 10.1016/0166-
1403 2236(90)90186-e.
1404 98. McCulloch, K.A., Zhou, K., and Jin, Y. (2020). Neuronal transcriptome analyses reveal novel
1405 neuropeptide modulators of excitation and inhibition imbalance in C. elegans. PLoS One
1406 *15*, e0233991. 10.1371/journal.pone.0233991.
1407 99. Teitler, M., and Herrick-Davis, K. (1994). Multiple serotonin receptor subtypes: molecular
1408 cloning and functional expression. Crit Rev Neurobiol *8*, 175-188.
1409 100. Knoedler, J.R., Inoue, S., Bayless, D.W., Yang, T., Tantry, A., Davis, C.H., Leung, N.Y.,
1410 Parthasarathy, S., Wang, G., Alvarado, M., et al. (2022). A functional cellular framework
1411 for sex and estrous cycle-dependent gene expression and behavior. Cell *185*, 654-671
1412 e622. 10.1016/j.cell.2021.12.031.
1413 101. Thakker-Varia, S., and Alder, J. (2009). Neuropeptides in depression: role of VGF. Behav
1414 Brain Res *197*, 262-278. 10.1016/j.bbr.2008.10.006.
1415 102. Andero, R., Dias, B.G., and Ressler, K.J. (2014). A role for Tac2, NkB, and Nk3 receptor in
1416 normal and dysregulated fear memory consolidation. Neuron *83*, 444-454.
1417 10.1016/j.neuron.2014.05.028.
1418 103. LeDuke, D.O., Borio, M., Miranda, R., and Tye, K.M. (2023). Anxiety and depression: A top-
1419 down, bottom-up model of circuit function. Ann N Y Acad Sci. 10.1111/nyas.14997.
1420 104. Kupcova, I., Danisovic, L., Grgac, I., and Harsanyi, S. (2022). Anxiety and Depression: What
1421 Do We Know of Neuropeptides? Behav Sci (Basel) *12*. 10.3390/bs12080262.
1422 105. Casello, S.M., Flores, R.J., Yarur, H.E., Wang, H., Awanyai, M., Arenivar, M.A., Jaime-Lara,
1423 R.B., Bravo-Rivera, H., and Tejeda, H.A. (2022). Neuropeptide System Regulation of
1424 Prefrontal Cortex Circuitry: Implications for Neuropsychiatric Disorders. Front Neural
1425 Circuits *16*, 796443. 10.3389/fncir.2022.796443.
1426 106. Ran, F.A., Cong, L., Yan, W.X., Scott, D.A., Gootenberg, J.S., Kriz, A.J., Zetsche, B., Shalem,
1427 O., Wu, X., Makarova, K.S., et al. (2015). In vivo genome editing using Staphylococcus
1428 aureus Cas9. Nature *520*, 186-191. 10.1038/nature14299.
1429 107. Li, Y., Mathis, A., Grewe, B.F., Osterhout, J.A., Ahanonu, B., Schnitzer, M.J., Murthy, V.N.,
1430 and Dulac, C. (2017). Neuronal Representation of Social Information in the Medial
1431 Amygdala of Awake Behaving Mice. Cell *171*, 1176-1190.e1117.
1432 10.1016/j.cell.2017.10.015.
1433 108. Straub, C., Granger, A.J., Saulnier, J.L., and Sabatini, B.L. (2014). CRISPR/Cas9-mediated
1434 gene knock-down in post-mitotic neurons. PLoS One *9*, e105584.
1435 10.1371/journal.pone.0105584.

1436 109. Hunker, A.C., Soden, M.E., Krayushkina, D., Heymann, G., Awatramani, R., and Zweifel,
1437 L.S. (2020). Conditional Single Vector CRISPR/SaCas9 Viruses for Efficient Mutagenesis in
1438 the Adult Mouse Nervous System. Cell Rep *30*, 4303-4316 e4306.
1439 10.1016/j.celrep.2020.02.092.
1440 110. Castro, D.C., Oswell, C.S., Zhang, E.T., Pedersen, C.E., Piantadosi, S.C., Rossi, M.A., Hunker,
1441 A.C., Guglin, A., Moron, J.A., Zweifel, L.S., et al. (2021). An endogenous opioid circuit
1442 determines state-dependent reward consumption. Nature *598*, 646-651.
1443 10.1038/s41586-021-04013-0.
1444 111. Soden, M.E., Yee, J.X., and Zweifel, L.S. (2023). Circuit coordination of opposing
1445 neuropeptide and neurotransmitter signals. Nature *619*, 332-337. 10.1038/s41586-023-
1446 06246-7.
1447 112. Swiech, L., Heidenreich, M., Banerjee, A., Habib, N., Li, Y., Trombetta, J., Sur, M., and
1448 Zhang, F. (2015). In vivo interrogation of gene function in the mammalian brain using
1449 CRISPR-Cas9. Nat Biotechnol *33*, 102-106. 10.1038/nbt.3055.
1450 113. Daigle, T.L., Madisen, L., Hage, T.A., Valley, M.T., Knoblich, U., Larsen, R.S., Takeno, M.M.,
1451 Huang, L., Gu, H., Larsen, R., et al. (2018). A Suite of Transgenic Driver and Reporter Mouse
1452 Lines with Enhanced Brain-Cell-Type Targeting and Functionality. Cell *174*, 465-480.e422.
1453 10.1016/j.cell.2018.06.035.
1454 114. Zhang, Y., and Looger, L.L. (2023). Fast and sensitive GCaMP calcium indicators for
1455 neuronal imaging. The Journal of physiology. 10.1113/JP283832.
1456 115. Stagkourakis, S., Spigolon, G., Liu, G., and Anderson, D.J. (2020). Experience-dependent
1457 plasticity in an innate social behavior is mediated by hypothalamic LTP. Proc Natl Acad Sci
1458 U S A *117*, 25789-25799. 10.1073/pnas.2011782117.
1459 116. Hong, W., Kennedy, A., Burgos-Artizzu, X.P., Zelikowsky, M., Navonne, S.G., Perona, P.,
1460 and Anderson, D.J. (2015). Automated measurement of mouse social behaviors using
1461 depth sensing, video tracking, and machine learning. Proc Natl Acad Sci U S A *112*, E5351-
1462 5360. 10.1073/pnas.1515982112.
1463 117. Segalin, C., Williams, J., Karigo, T., Hui, M., Zelikowsky, M., Sun, J.J., Perona, P., Anderson,
1464 D.J., and Kennedy, A. (2021). The Mouse Action Recognition System (MARS) software
1465 pipeline for automated analysis of social behaviors in mice. Elife *10*. 10.7554/eLife.63720.
1466 118. Lerner, T.N., Shilyansky, C., Davidson, T.J., Evans, K.E., Beier, K.T., Zalocusky, K.A., Crow,
1467 A.K., Malenka, R.C., Luo, L., Tomer, R., and Deisseroth, K. (2015). Intact-Brain Analyses
1468 Reveal Distinct Information Carried by SNc Dopamine Subcircuits. Cell *162*, 635-647.
1469 10.1016/j.cell.2015.07.014.
1470 119. Zhou, P., Resendez, S.L., Rodriguez-Romaguera, J., Jimenez, J.C., Neufeld, S.Q.,
1471 Giovannucci, A., Friedrich, J., Pnevmatikakis, E.A., Stuber, G.D., Hen, R., et al. (2018).
1472 Efficient and accurate extraction of in vivo calcium signals from microendoscopic video
1473 data. Elife *7*. 10.7554/eLife.28728.
1474 120. Shadlen, M.N., Britten, K.H., Newsome, W.T., and Movshon, J.A. (1996). A computational
1475 analysis of the relationship between neuronal and behavioral responses to visual motion.
1476 J Neurosci *16*, 1486-1510. 10.1523/JNEUROSCI.16-04-01486.1996.
1477 121. Maheswaranathan, N., Williams, A.H., Golub, M.D., Ganguli, S., and Sussillo, D. (2019).
1478 Reverse engineering recurrent networks for sentiment classification reveals line attractor
1479 dynamics. Adv Neural Inf Process Syst *32*, 15696-15705.

1480

Figure 1

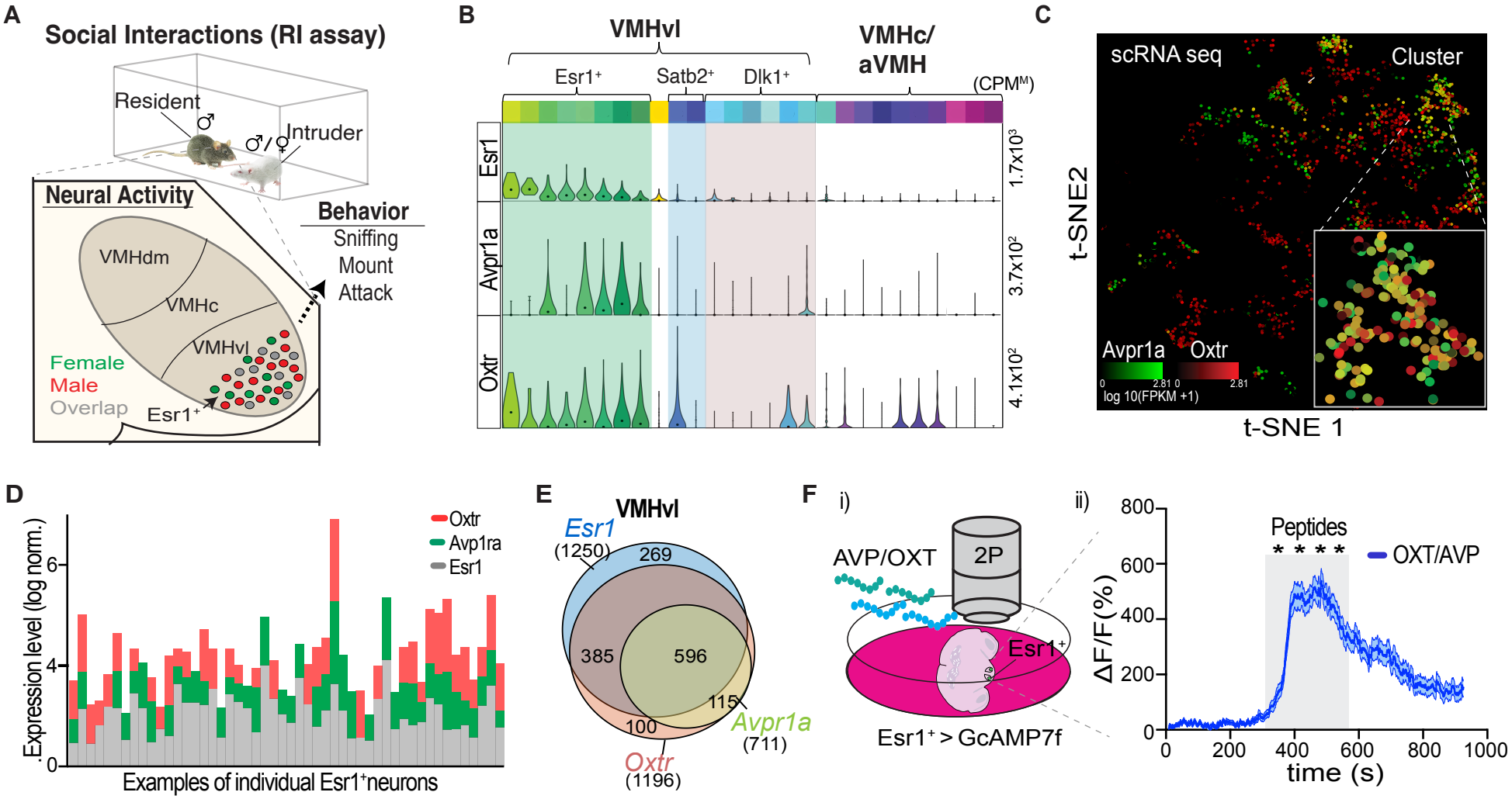
A
Social Interactions (RI assay)
Resident
♂/♀
Intruder
Neural Activity
VMHdm
VMHc
VMHvl
Female
Male
Overlap
Esr1+
Behavior
Sniffing
Mount
Attack
B
VMHvl
VMHc/
aVMH
Esr1+
Satb2+
Dlk1+
(CPMM)
Esr1
Avpr1a
Oxtr
1.7x10³
3.7x10²
4.1x10²
C
scRNA seq
Cluster
t-SNE2
t-SNE 1
Avpr1a
Oxtr
log 10(FPKM +1)
D
Expression level (log norm.)
Oxtr
Avp1ra
Esr1
Examples of individual Esr1+neurons
E
VMHvl
Esr1
(1250)
269
385
596
115
100
Avpr1a
(711)
Oxtr
(1196)
F
i)
AVP/OXT
2P
Esr1+
Esr1+ > GcAMP7f
ii)
Peptides
OXT/AVP
ΔF/F(%)
time (s)

Figure 2

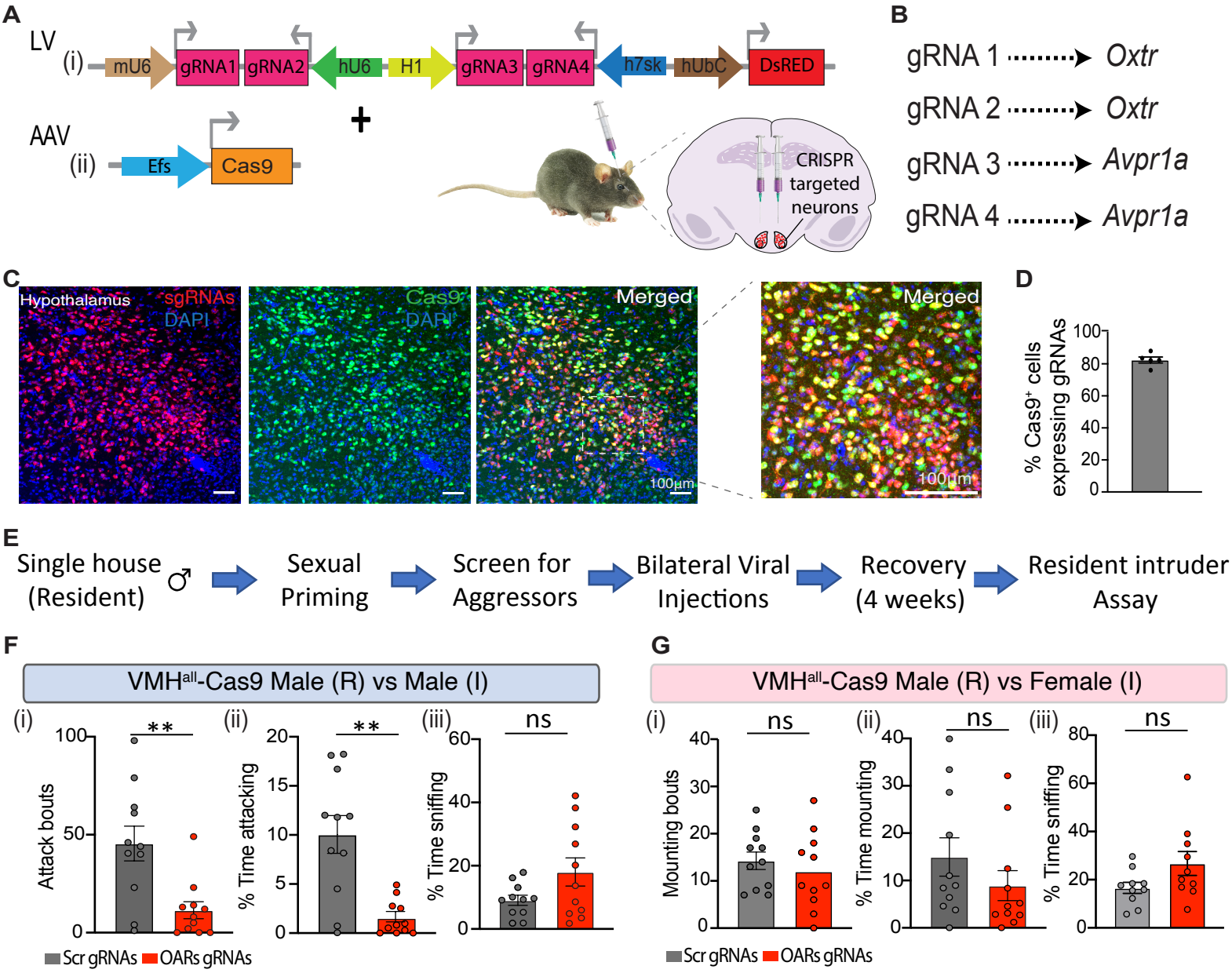
A
LV
(i)
mU6
gRNA1
gRNA2
hU6
H1
gRNA3
gRNA4
h7sk
hUbC
DsRED
AAV
(ii)
Efs
Cas9
+
CRISPR targeted neurons
B
gRNA 1 → Oxtr
gRNA 2 → Oxtr
gRNA 3 → Avpr1a
gRNA 4 → Avpr1a
C
Hypothalamus
sgRNAs
DAPI
Cas9
DAPI
Merged
100µm
Merged
100µm
D
% Cas9+ cells expressing gRNAs
100
80
60
40
20
0
E
Single house (Resident) ♂
Sexual Priming
Screen for Aggressors
Bilateral Viral Injections
Recovery (4 weeks)
Resident intruder Assay
F
VMHall-Cas9 Male (R) vs Male (I)
(i)
Attack bouts
100
50
0
**
(ii)
% Time attacking
20
15
10
5
0
**
(iii)
% Time sniffing
60
40
20
0
ns
Scr gRNAs
OARs gRNAs
G
VMHall-Cas9 Male (R) vs Female (I)
(i)
Mounting bouts
40
30
20
10
0
ns
(ii)
% Time mounting
40
30
20
10
0
ns
(iii)
% Time sniffing
80
60
40
20
0
ns
Scr gRNAs
OARs gRNAs

Figure 3

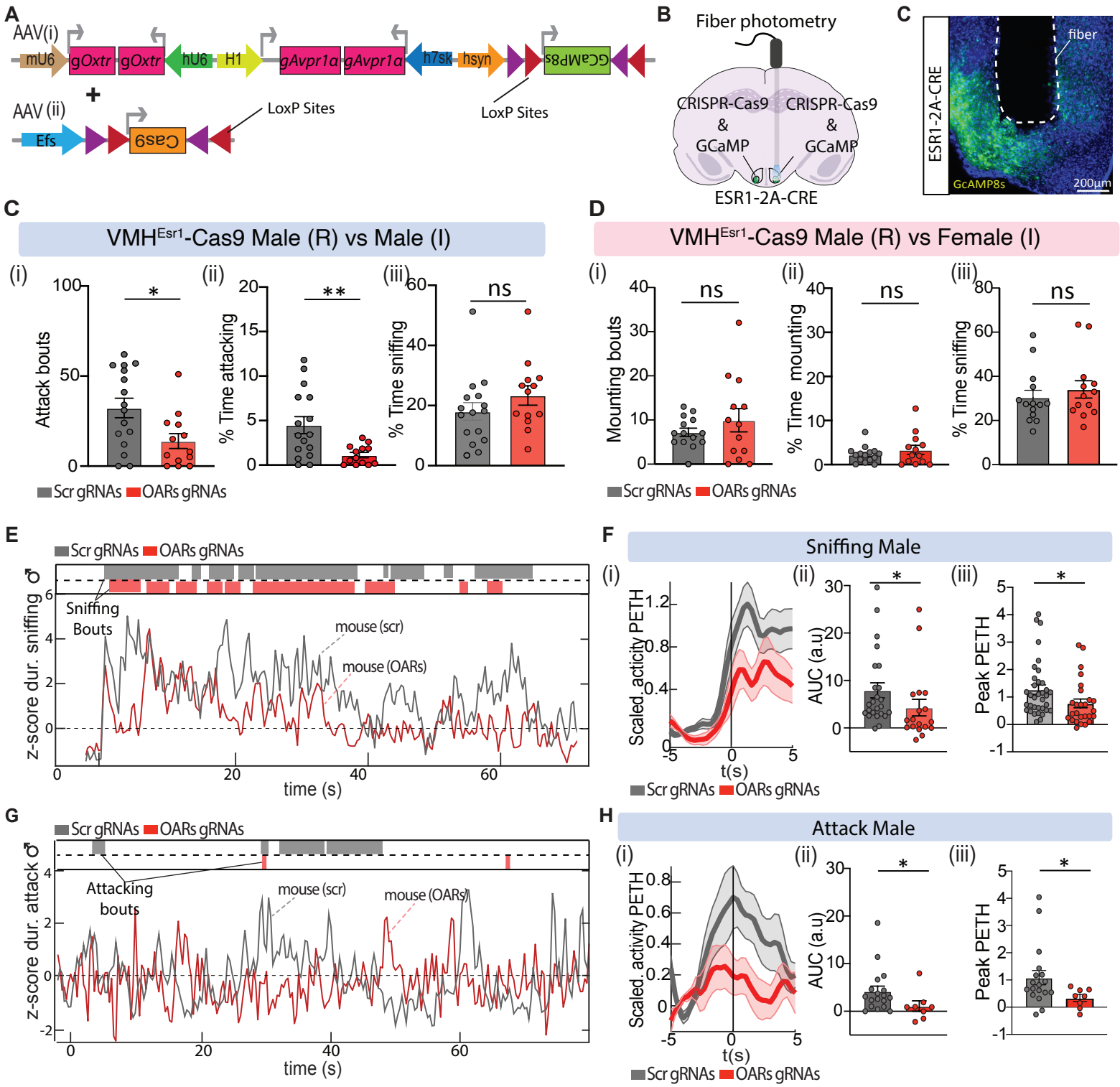
A
AAV(i)
mU6
gOxtr
gOxtr
hU6
H1
gAvpr1a
gAvpr1a
h7sk
hsyn
GCaMP8s
+
AAV (ii)
Efs
Cas9
LoxP Sites
LoxP Sites
B
Fiber photometry
CRISPR-Cas9 & GCaMP
CRISPR-Cas9 & GCaMP
ESR1-2A-CRE
C
ESR1-2A-CRE
fiber
GcAMP8s
200µm
C
VMH^Esr1-Cas9 Male (R) vs Male (I)
(i)
Attack bouts
*
(ii)
% Time attacking
**
(iii)
% Time sniffing
ns
Scr gRNAs
OARs gRNAs
D
VMH^Esr1-Cas9 Male (R) vs Female (I)
(i)
Mounting bouts
ns
(ii)
% Time mounting
ns
(iii)
% Time sniffing
ns
Scr gRNAs
OARs gRNAs
E
Scr gRNAs
OARs gRNAs
Sniffing Bouts
mouse (scr)
mouse (OARs)
z-score dur. sniffing ♂
time (s)
F
Sniffing Male
(i)
Scaled acticity PETH
t(s)
(ii)
AUC (a.u)
*
(iii)
Peak PETH
*
Scr gRNAs
OARs gRNAs
G
Scr gRNAs
OARs gRNAs
Attacking bouts
mouse (scr)
mouse (OARs)
z-score dur. attack ♂
time (s)
H
Attack Male
(i)
Scaled activity PETH
t(s)
(ii)
AUC (a.u)
*
(iii)
Peak PETH
*
Scr gRNAs
OARs gRNAs

Figure 4

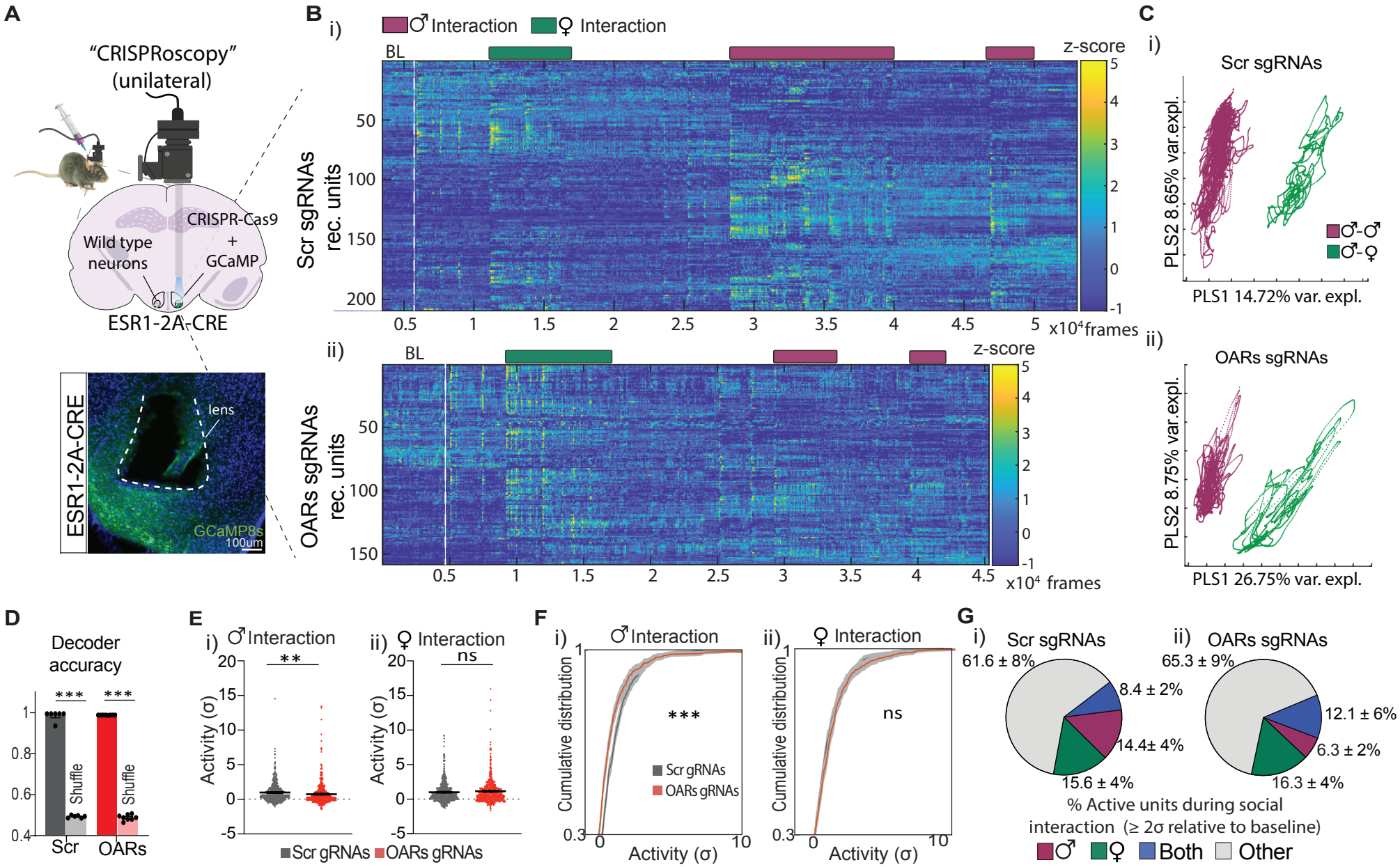
A
"CRISPRoscopy"
(unilateral)
CRISPR-Cas9
+
GCaMP
Wild type
neurons
ESR1-2A-CRE
ESR1-2A-CRE
lens
GCaMP8s
100um
B
i)
♂ Interaction
♀ Interaction
BL
z-score
Scr sgRNAs
rec. units
x10⁴frames
ii)
OARs sgRNAs
rec. units
x10⁴ frames
C
i)
Scr sgRNAs
PLS2 8.65% var.expl.
PLS1 14.72% var. expl.
♂-♂
♂-♀
ii)
OARs sgRNAs
PLS2 8.75% var.expl.
PLS1 26.75% var. expl.
D
Decoder
accuracy
Scr
OARs
Shuffle
E
i) ♂ Interaction
ii) ♀ Interaction
Activity (σ)
Scr gRNAs
OARs gRNAs
F
i) ♂ Interaction
ii) ♀ Interaction
Cumulative distribution
Activity (σ)
Scr gRNAs
OARs gRNAs
G
i) Scr sgRNAs
ii) OARs sgRNAs
61.6 ± 8%
8.4 ± 2%
14.4± 4%
15.6 ± 4%
65.3 ± 9%
12.1 ± 6%
6.3 ± 2%
16.3 ± 4%
% Active units during social
interaction (≥ 2σ relative to baseline)
♂ ♀ Both Other

Figure 5

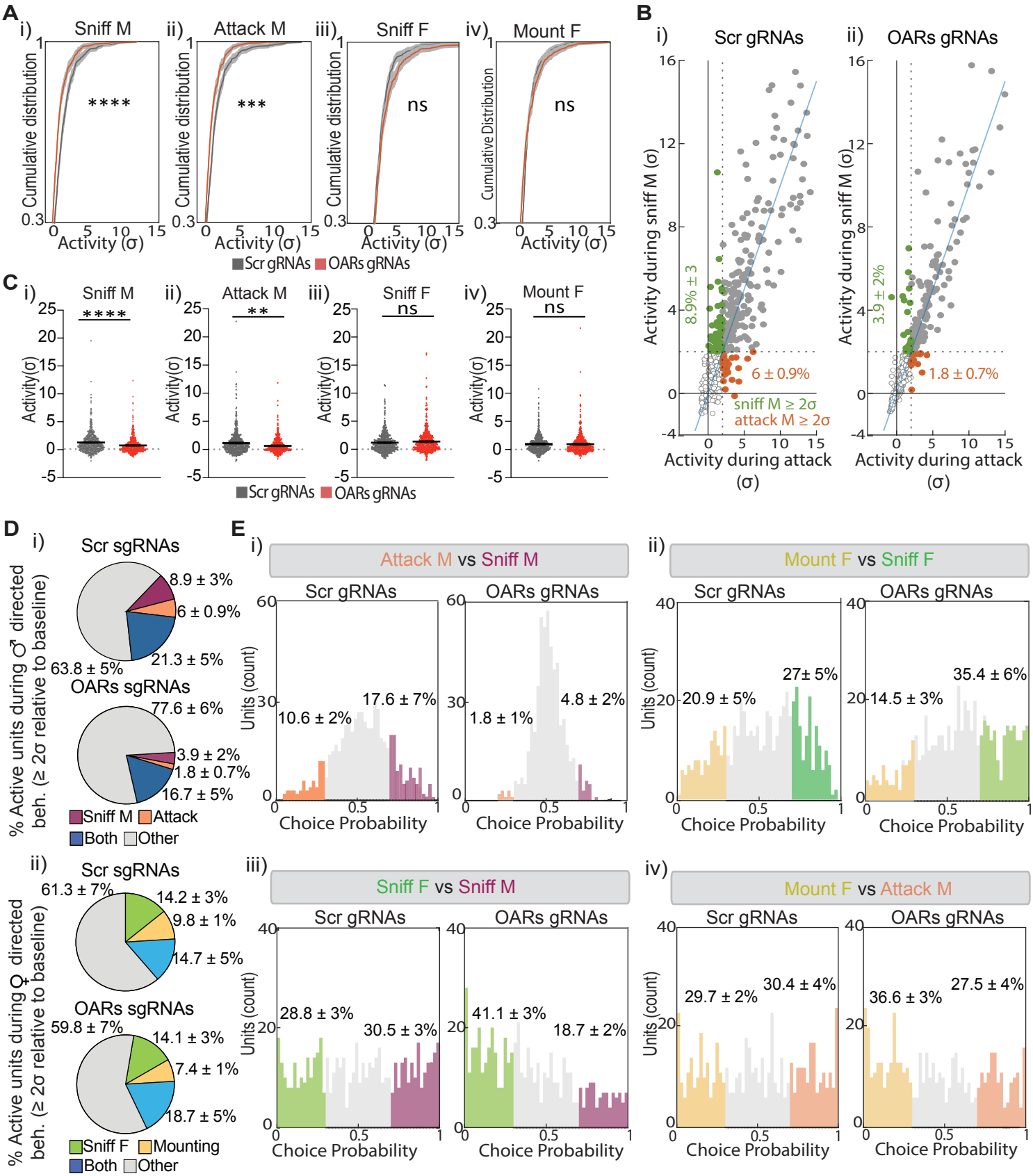
A
i) Sniff M
ii) Attack M
iii) Sniff F
iv) Mount F
Cumulative distribution
Cumulative Distribution
****
***
ns
ns
Activity (σ)
Scr gRNAs
OARs gRNAs
B
i) Scr gRNAs
ii) OARs gRNAs
Activity during sniff M (σ)
Activity during attack (σ)
8.9% ± 3
6 ± 0.9%
sniff M ≥ 2σ
attack M ≥ 2σ
3.9 ± 2%
1.8 ± 0.7%
C
i) Sniff M
ii) Attack M
iii) Sniff F
iv) Mount F
Activity(σ)
****
**
ns
ns
Scr gRNAs
OARs gRNAs
D
i)
Scr sgRNAs
8.9 ± 3%
6 ± 0.9%
21.3 ± 5%
63.8 ± 5%
OARs sgRNAs
77.6 ± 6%
3.9 ± 2%
1.8 ± 0.7%
16.7 ± 5%
Sniff M
Attack
Both
Other
% Active units during ♂ directed beh. (≥ 2σ relative to baseline)
ii)
Scr sgRNAs
61.3 ± 7%
14.2 ± 3%
9.8 ± 1%
14.7 ± 5%
OARs sgRNAs
59.8 ± 7%
14.1 ± 3%
7.4 ± 1%
18.7 ± 5%
Sniff F
Mounting
Both
Other
% Active units during ♀ directed beh. (≥ 2σ relative to baseline)
E
i) Attack M vs Sniff M
Scr gRNAs
OARs gRNAs
10.6 ± 2%
17.6 ± 7%
1.8 ± 1%
4.8 ± 2%
ii) Mount F vs Sniff F
20.9 ± 5%
27± 5%
14.5 ± 3%
35.4 ± 6%
iii) Sniff F vs Sniff M
28.8 ± 3%
30.5 ± 3%
41.1 ± 3%
18.7 ± 2%
iv) Mount F vs Attack M
29.7 ± 2%
30.4 ± 4%
36.6 ± 3%
27.5 ± 4%
Units (count)
Choice Probability

Figure 6

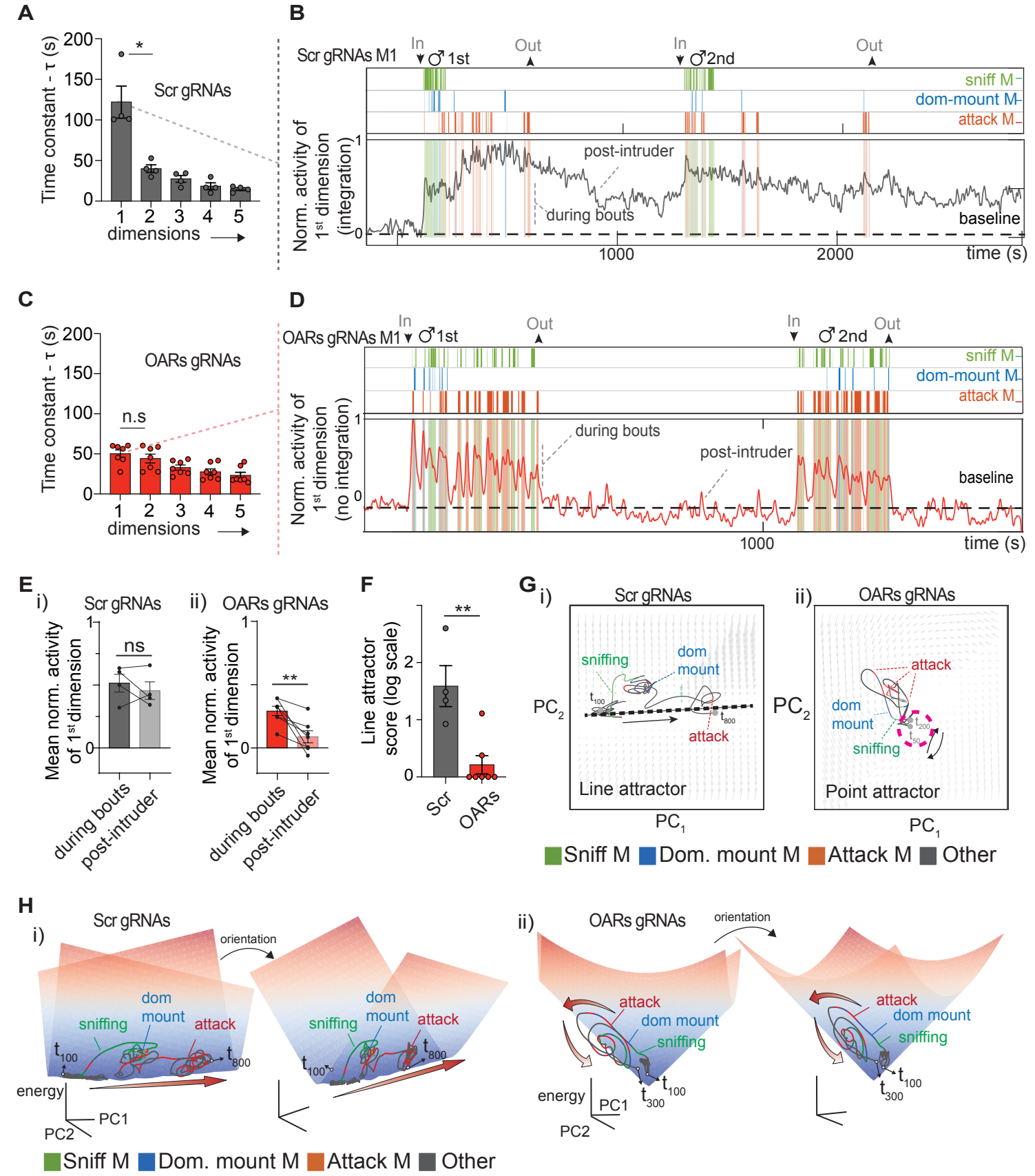
A
Time constant - τ (s)
200
150
100
50
0
*
Scr gRNAs
1 2 3 4 5
dimensions
B
Scr gRNAs M1
In
♂1st
Out
In
♂2nd
Out
sniff M
dom-mount M
attack M
Norm. activity of 1st dimension (integration)
1
0
post-intruder
during bouts
baseline
1000
2000
time (s)
C
Time constant - τ (s)
200
150
100
50
0
OARs gRNAs
n.s
1 2 3 4 5
dimensions
D
OARs gRNAs M1
In
♂1st
Out
In
♂2nd
Out
sniff M
dom-mount M
attack M
Norm. activity of 1st dimension (no integration)
1
0
during bouts
post-intruder
baseline
1000
time (s)
E
i)
Scr gRNAs
Mean norm. activity of 1st dimension
1
0
ns
during bouts
post-intruder
ii)
OARs gRNAs
Mean norm. activity of 1st dimension
1
0
**
during bouts
post-intruder
F
Line attractor score (log scale)
2
1
0
**
Scr
OARs
G
i)
Scr gRNAs
sniffing
dom mount
attack
PC2
PC1
Line attractor
ii)
OARs gRNAs
attack
dom mount
sniffing
PC2
PC1
Point attractor
Sniff M
Dom. mount M
Attack M
Other
H
i)
Scr gRNAs
orientation
dom mount
sniffing
attack
energy
PC1
PC2
ii)
OARs gRNAs
orientation
attack
dom mount
sniffing
energy
PC1
PC2
Sniff M
Dom. mount M
Attack M
Other

Figure 7

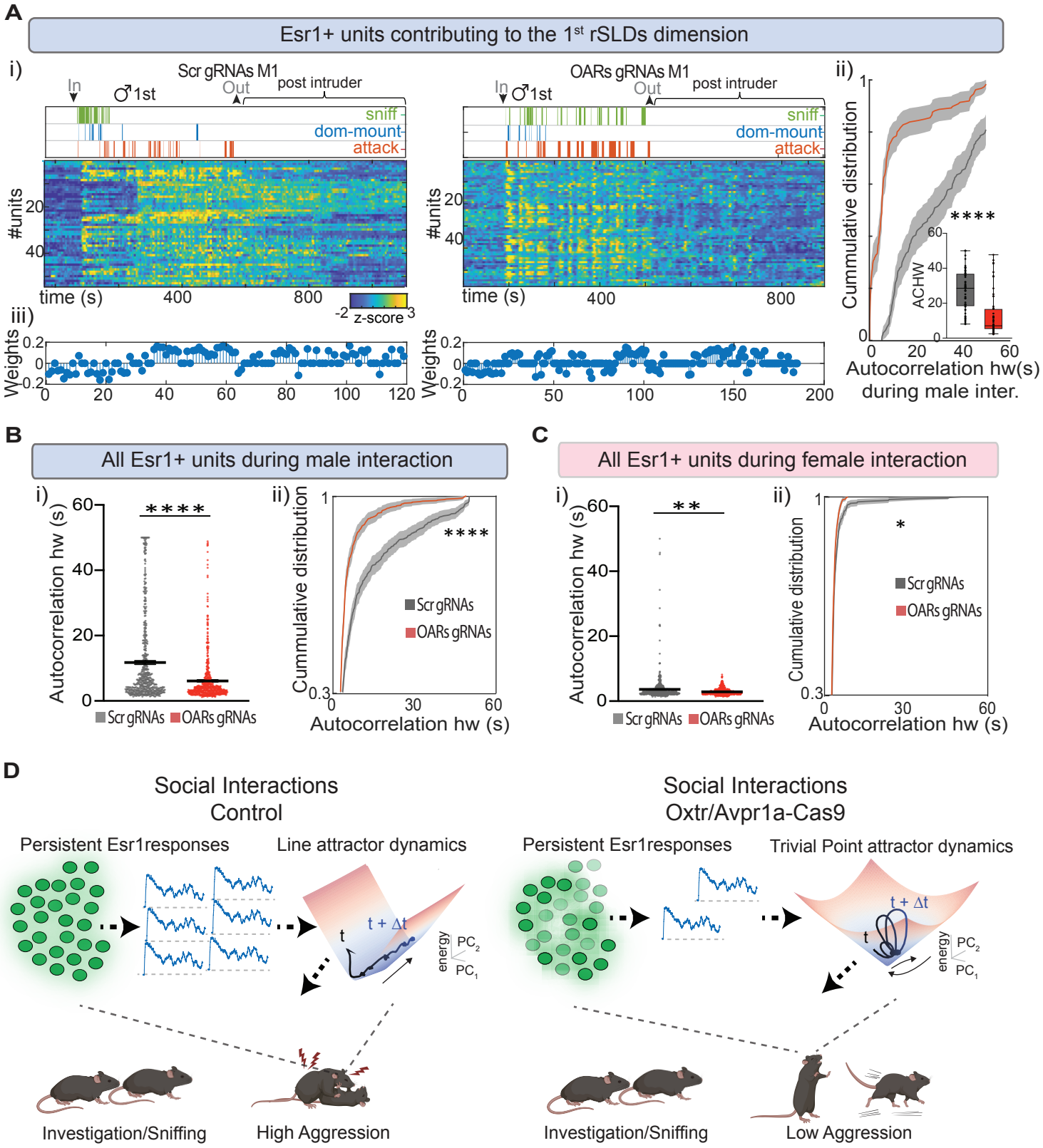
A
Esr1+ units contributing to the 1st rSLDs dimension
i)
Scr gRNAs M1
In
♂1st
Out
post intruder
sniff
dom-mount
attack
#units
time (s)
z-score
OARs gRNAs M1
ii)
Cummulative distribution
ACHW
****
Autocorrelation hw(s) during male inter.
iii)
Weights
B
All Esr1+ units during male interaction
Autocorrelation hw (s)
Scr gRNAs
OARs gRNAs
Cummulative distribution
C
All Esr1+ units during female interaction
**
*
D
Social Interactions Control
Persistent Esr1responses
Line attractor dynamics
t + Δt
energy
PC2
PC1
Investigation/Sniffing
High Aggression
Social Interactions Oxtr/Avpr1a-Cas9
Trivial Point attractor dynamics
Low Aggression